How Does the Relationship between Ambient Deep-Tropospheric Vertical Wind Shear and Tropical Cyclone Tornadoes Change between Coastal and Inland Environments?

BENJAMIN A. SCHENKEL,[a,b] MICHAEL CONIGLIO,[b] AND ROGER EDWARDS[c]

[a] *Cooperative Institute for Mesoscale Meteorological Studies, School of Meteorology, University of Oklahoma, Norman, Oklahoma*
[b] *NOAA/NSSL, Norman, Oklahoma*
[c] *NOAA/SPC, Norman, Oklahoma*

(Manuscript received 23 July 2020, in final form 11 January 2021)

ABSTRACT: This work investigates how the relationship between tropical cyclone (TC) tornadoes and ambient (i.e., synoptic-scale) deep-tropospheric (i.e., 850–200-hPa) vertical wind shear (VWS) varies between coastal and inland environments. Observed U.S. TC tornado track data are used to study tornado frequency and location, while dropsonde and radiosonde data are used to analyze convective-scale environments. To study the variability in the TC tornado–VWS relationship, these data are categorized by both 1) their distance from the coast and 2) reanalysis-derived VWS magnitude. The analysis shows that TCs produce coastal tornadoes regardless of VWS magnitude primarily in their downshear sector, with tornadoes most frequently occurring in strongly sheared cases. Inland tornadoes, including the most damaging cases, primarily occur in strongly sheared TCs within the outer radii of the downshear-right quadrant. Consistent with these patterns, dropsondes and coastal radiosondes show that the downshear-right quadrant of strongly sheared TCs has the most favorable combination of enhanced lower-tropospheric near-surface speed shear and veering, and reduced lower-tropospheric thermodynamic stability for tornadic supercells. Despite the weaker intensity farther inland, these kinematic conditions are even more favorable in inland environments within the downshear-right quadrant of strongly sheared TCs, due to the strengthened veering of the ambient winds and the lack of changes in the TC outer tangential wind field strength. The constructive superposition of the ambient and TC winds may be particularly important to inland tornado occurrence. Together, these results will allow forecasters to anticipate how the frequency and location of tornadoes and, more broadly, convection may change as TCs move inland.

KEYWORDS: Tornadoes; Tropical cyclones; Climatology; Hurricanes/typhoons; Dropsondes; Radiosonde/rawinsonde observations

1. Introduction

Landfalling tropical cyclones (TCs) are associated with multiple hazards including damaging winds, flooding, storm surge, and tornadoes (Blake and Zelinsky 2018; Cangialosi et al. 2018). Of these hazards, tornadoes are among the least studied. Prior work has shown tornadoes typically occur in the northeast quadrant of landfalling TCs within 100–500 km from the storm center. Moreover, most of these tornadoes are associated with light-to-moderate damage (i.e., EF/F scale between 0 and 1; McCaul 1991; Schultz and Cecil 2009). TC tornado convective-scale environments are typically characterized by strong lower-tropospheric vertical wind shear with enhanced convective cell-relative helicity and sufficient lower-tropospheric thermodynamic instability (McCaul 1991; Edwards et al. 2012). TC convective-scale environments are typically more favorable for tornadoes in the following conditions: 1) during the afternoon, especially in the outer rainbands (Novlan and Gray 1974; Edwards and Thompson 2012), 2) during the 48 h before and after landfall typically within 100 km of the coast (Hill et al. 1966; Schultz and Cecil 2009), and 3) in TCs within environments characterized by strong ambient (i.e., synoptic-scale) deep-tropospheric (i.e., 850–200-hPa) vertical wind shear (VWS; hereafter, VWS will refer to synoptic-scale deep-tropospheric values for each TC, as opposed to the mid- or lower troposphere; Verbout et al. 2007; Schenkel et al. 2020). However, we still do not completely understand why only some TCs produce inland tornado outbreaks (Edwards 2012). This may be due to most previous studies considering these above conditions in isolation from one another, despite their interdependence (e.g., postlandfall TCs weaken and encounter increasingly stronger VWS; Aiyyer and Thorncroft 2006; Chen et al. 2006). The present study will focus on how the relationship between TC tornado occurrence and VWS changes, if at all, between coastal versus inland environments.

To understand how the impact of VWS on tornado production may differ between coastal and inland environments, we must first consider how a typical TC that produces tornadoes both at landfall and inland environments responds as its synoptic-scale environment changes as summarized in Fig. 1. As the TC approaches the coast (Fig. 1a), its supercells tend to intensify and produce tornadoes upon moving inland in response to enhanced lower-tropospheric convective

Supplemental information related to this paper is available at the Journals Online website: https://doi.org/10.1175/WAF-D-20-0127.s1.

Corresponding author: Benjamin A. Schenkel, benschenkel@gmail.com

DOI: 10.1175/WAF-D-20-0127.1

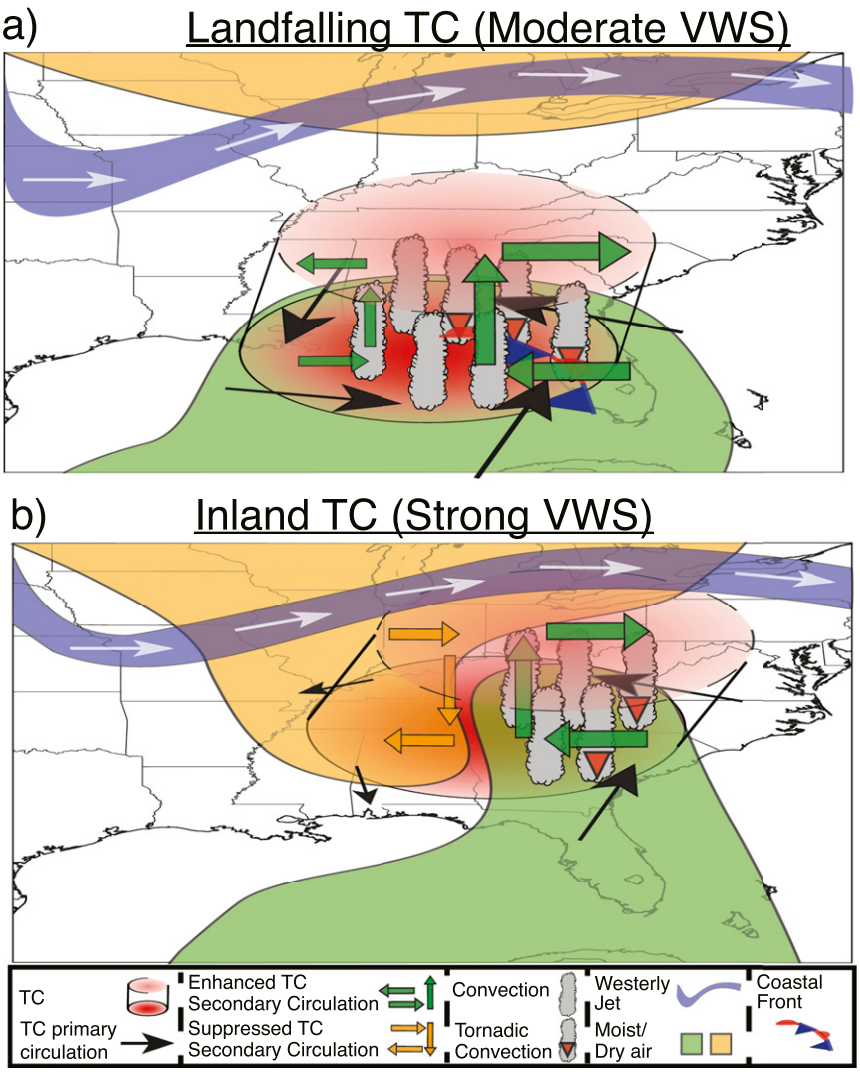

FIG. 1. Three-dimensional schematic showing hypothetical TC that produces tornadoes both (a) at landfall in moderate-to-strong VWS and (b) inland in strong VWS based upon prior work (McCaul 1991; Schenkel et al. 2020).

cell-relative helicity over land, compared to the ocean due to enhanced surface friction (Baker et al. 2009; Eastin and Link 2009). Additionally, any preexisting coastal fronts or baroclinic zones may be further enhanced by the convergent, cyclonic wind field of the TC during landfall, providing a mesoscale region of enhanced convective-scale vertical wind shear, reduced stability, and lift near the coast that is advected inland by the eastern flank of the TC (Knupp et al. 2006; Green et al. 2011). Following landfall, TC intensity typically weakens as the storm is displaced from its oceanic energy source (Kaplan and DeMaria 1995; Chen and Chavas 2020), which should contribute to reduced convective-scale vertical wind shear and less favorable tornadic environments (Novlan and Gray 1974; Gentry 1983).

Finally, landfalling TCs typically occur in moderate-to-strong westerly VWS, which enhances convective-scale lower-tropospheric vertical wind shear in TCs and, ultimately, the likelihood of tornadogenesis (Molinari and Vollaro 2008; Schenkel et al. 2020). The strongest vertical shears in the ambient winds occur within the mid-to-upper troposphere in association with the subtropical or polar jet (Verbout et al. 2007; Finocchio and Majumdar 2017), which can impact TC intensity and symmetry due to the TC circulation extending throughout the troposphere (Simpson and Riehl 1958; Marks et al. 1992). There are two hypotheses for how VWS creates favorable convective-scale environments for TC tornadoes. First, VWS tilts the TC circulation in the direction of the VWS vector with height, which enhances the TC secondary circulation (i.e., lower-tropospheric inflow, ascent near TC center, and upper-tropospheric outflow) in the downshear half of the TC (i.e., half of the TC in the direction of VWS vector; Jones 1995; Frank and Ritchie 1999). The VWS-induced

downshear enhancement of the TC secondary circulation is associated with more favorable convective-scale vertical wind shear and enhanced tropospheric moisture for tornadic supercells relative to the upshear half of the TC (Molinari and Vollaro 2008; J. Zhang et al. 2013). Conversely, the upshear half (i.e., direction against the VWS vector) of the TC is characterized by a suppressed secondary circulation and unfavorable convective-scale environments for tornadic supercells (Molinari and Vollaro 2008; Schenkel et al. 2020). The second factor is the constructive superposition between the veering of the ambient and TC winds, which nonlinearly enhances the helicity of the total wind (i.e., ambient plus TC) beyond the sum of the ambient and TC winds computed independently. This most strongly occurs within the quadrant that is in the same direction and to the right of the VWS vector (i.e., downshear-right quadrant; Schenkel et al. 2020). Together, these two factors suggest both the magnitude and vertical structure of ambient winds are key details in determining whether interactions between VWS and the TC can create sufficient convective-scale helicity to support tornadoes (McCaul 1991; Schenkel et al. 2020). Moreover, these factors suggest that tornado production should be greatest immediately at the coast within the downshear sector before the TC weakens.

After landfall (Fig. 1b), the TC wind field continues to weaken as the storm moves farther inland. Warm, moist onshore flow is increasingly concentrated in the eastern half of the TC, while dry, midtropospheric continental dry air is entrained on its western half (Novlan and Gray 1974; Curtis 2004). Additionally, the TC may encounter increased westerly VWS as it moves poleward closer to the climatological location of the subtropical or polar jet (Aiyyer and Thorncroft 2006; Verbout et al. 2007). This increased VWS hastens the postlandfall weakening of the TC by more efficiently entraining cooler, drier environmental air into its warm core (Simpson and Riehl 1958; Tang and Emanuel 2010). This weakening of the TC should also reduce convective-scale vertical wind shear. However, this decrease in convective-scale helicity may be counterbalanced in the downshear quadrants by stronger tilting of the TC as it weakens and moves poleward. This enhanced vertical tilting may further accelerate the TC secondary circulation, and partially offset the aforementioned helicity decreases (Jones 1995; Reasor et al. 2004). Moreover, stronger VWS in inland environments may also be associated with enhanced lower-tropospheric ambient vertical wind shear that may constructively superimpose with the TC winds in the downshear-right quadrant to further counter the reduced helicity associated with the weakening TC (Molinari and Vollaro 2008; Schenkel et al. 2020). Last, strong VWS and its associated strong ambient baroclinicity may facilitate the extratropical transition of inland TCs, which occurs for ~50% of North Atlantic storms (Hart and Evans 2001; Bieli et al. 2019). Extratropical transition is associated with warm conveyor belt development downstream of the TC (Klein et al. 2000; Ritchie and Elsberry 2001), which may enhance their convective-scale kinematic environments. However, prior work has shown that VWS remains the primary factor influencing TC convective symmetry and strength even during the early part of transition (Foerster et al. 2014; Quinting et al. 2014). Indeed, the two most prolific tornado producing TCs in the modern record, Hurricane Ivan and Frances (2004), both produced the majority of their tornadoes in the 1–2 days preceding the end of extratropical transition (Knapp et al. 2010; Edwards 2012). Together, these results suggest that tornado production may decrease while becoming more concentrated downshear as the TC moves inland. However, the response of convective-scale environments is sensitive to: 1) how the vertical structure of VWS changes and 2) changes in the TC wind field due to any variation in VWS and increasing land interaction.

While Fig. 1 provides a framework for understanding how tornado production may typically change as TCs move inland, few studies have systematically tested how these aforementioned factors may interact (McCaul 1991; Schultz and Cecil 2009). Hence, this study investigates how the sensitivity of TC tornado occurrence and convective-scale environments to VWS changes between coastal versus inland environments. Specifically, multidecadal U.S. tornado data are used to quantify how the sensitivity of tornado occurrence to reanalysis-derived VWS data changes, if at all, between coastal and inland environments. We will then use thousands of dropsondes and

TABLE 1. Sample sizes of tornadoes and uniquely named TCs producing tornadoes in strong, moderate, and weak VWS. The same TC may contribute multiple 6-h times to multiple VWS categories such that the sum of the number of TCs in each VWS regime does not equal the number in the All VWS category.

	No. of tornadoes	No. of TCs
All VWS	1304	90
Strong VWS	695	62
Moderate VWS	401	53
Weak VWS	208	30

TABLE 2. List of data sources and citations from which dropsondes are collected in this study.

Dropsonde source	Citation
NOAA-DHA Long-term Dropsonde Hurricane archive	Wang et al. (2015)
NOAA Intensity Forecasting Experiment (IFEX)	Rogers et al. (2006, 2013)
NSF Hurricane Rainband and Intensity Change Experiment (RAINEX)	Houze et al. (2006)
NASA Genesis and Rapid Intensification Processes (GRIP)	Braun et al. (2013)
NSF Pre-Depression Investigation of Cloud-systems in the Tropics (PREDICT)	Montgomery et al. (2012)
NASA Hurricane and Severe Storm Sentinel (HS3)	Braun et al. (2016)
NOAA and NSF Sensing Hazards with Operational Unmanned Technology (SHOUT)	Dunion et al. (2018)
NASA East Pacific Origins and Characteristics of Hurricanes (EPOCH; also sampled Atlantic TCs)	Emory et al. (2015)

TABLE 3. Number of radiosondes and dropsondes, and uniquely named TCs sampled by radiosondes and dropsondes for all, strongly sheared, moderately sheared, and weakly sheared TCs. The same TC may be sampled by multiple dropsondes and radiosondes such that the number of TCs sampled by radiosondes in weak, moderate, and strong VWS does not equal the number in the all VWS category.

	No. of radiosondes	No. of dropsondes	No. of TCs sampled by radiosondes	No. of TCs sampled by dropsondes
All VWS	8470	4427	406	94
Strong VWS	2930	904	284	44
Moderate VWS	3300	1870	315	68
Weak VWS	2240	1653	239	59

radiosondes to diagnose statistical differences in convective-scale kinematic and thermodynamic environments associated with these changes in tornado occurrence. Specifically, this study will address the following questions:

- Are tornadoes increasingly located downshear as TCs move inland into more strongly sheared environments?
- Does VWS also impact the number of tornadoes produced at the coast by TCs?
- Is strong VWS a necessary ingredient for inland tornado production by TCs?
- How do convective-scale environments change due to weaker TC intensity and typically stronger VWS in inland environments?

Together, this work will provide a more nuanced understanding of how VWS impacts tornadoes and, more broadly, deep convection as TCs move inland.

2. Data and methods

a. Tornado and TC data

The 25-yr (1995–2019) SPC TC tornado data (TCTOR; Edwards 2010) are used for examining the starting location, date, and damage category for tornadoes in the continental United States (CONUS). While different from one another, the F scale used to estimate damage before 2007 and the EF scale used thereafter in TCTOR are intended to calibrate well to one another to avoid climatological shocks with the introduction of the EF scale (Edwards et al. 2013). Each tornado has been subjectively verified to be associated with a TC using several different observation sources (e.g., WSR-88D and observational charts), and modern tornado verification processes (Edwards 2010). We collocate these tornado data with 6-h TC track data from the National Hurricane Center best track as given in International Best Track Archive for Climate Stewardship (IBTRaCS), version 4 (Knapp et al. 2010). We include all 6-h IBTrACS times for TCs that are classified as tropical (i.e., not subtropical or extratropical; $N = 1304$ tornadoes in 90 TCs), and are of tropical depression strength or stronger. IBTRaCS data are temporally interpolated using a piecewise cubic Hermite polynomial to the time of tornadogenesis (Chavas and Vigh 2014).

b. VWS data

VWS is calculated using data from the 6-h 0.25° × 0.25° ECMWF fifth-generation reanalysis (ERA5) available from 1979 to 2019 (Hersbach et al. 2020). Reanalysis TC track and outer wind field structure and size are well represented (Schenkel and Hart 2012; Schenkel et al. 2017), and have been used extensively to calculate VWS (Tang and Emanuel 2012; Rios-Berrios and Torn 2017) including for TC tornadoes (Schenkel et al. 2020). Instead of assuming the reanalysis TC is located at the IBTrACS TC location when calculating VWS, we use a vortex recentering algorithm (Brammer 2017) to identify the reanalysis TC location prior to computing VWS. This methodology is similar to the GFDL operational tracker (Marchok 2002), and has been employed in prior work (Brammer and Thorncroft 2017; Schenkel et al. 2017). Vortex recentering is necessitated by the nontrivial uncertainties in TC location within reanalyses (Schenkel and Hart 2012; Hodges et al. 2017) and, to a lesser extent, IBTrACS (Torn and Snyder 2012; Landsea and Franklin 2013). The recentering algorithm consists of two steps: 1) use the 6-h IBTrACS TC location as a first guess and 2) calculate the reanalysis TC location about the IBTrACS position as the mean of the center of mass of mean sea level pressure, 925-, 850-, and 700-hPa relative vorticity, and 850- and 700-hPa geopotential height (Brammer 2017; Marchok 2002).

Using the TC tracker position, VWS is calculated by removing the TC wind field from the reanalysis and then computing the vertical wind shear over the 850–200-hPa layer in three steps (Davis et al. 2008; Galarneau and Davis 2013).

- Solve a Poisson equation with uniform boundary conditions over a 500-km radius from the objectively derived TC center (e.g., approximate median TC outer size; Chavas and Emanuel 2010; Schenkel et al. 2018) to obtain the nondivergent and irrotational components of the TC wind field at 200 and 850 hPa;

TABLE 4. Number of radiosondes and uniquely named TCs sampled by radiosondes in all cases, and coastal, transition, and inland environments. The same TC may be sampled by multiple radiosondes such that the number of TCs sampled by radiosondes in coastal, transition, and inland environments does not equal the number in the all environments category.

	No. of radiosondes	No. of TCs sampled by radiosondes
All environments	8470	406
Coastal	5138	404
Transition	1451	205
Inland	1881	168

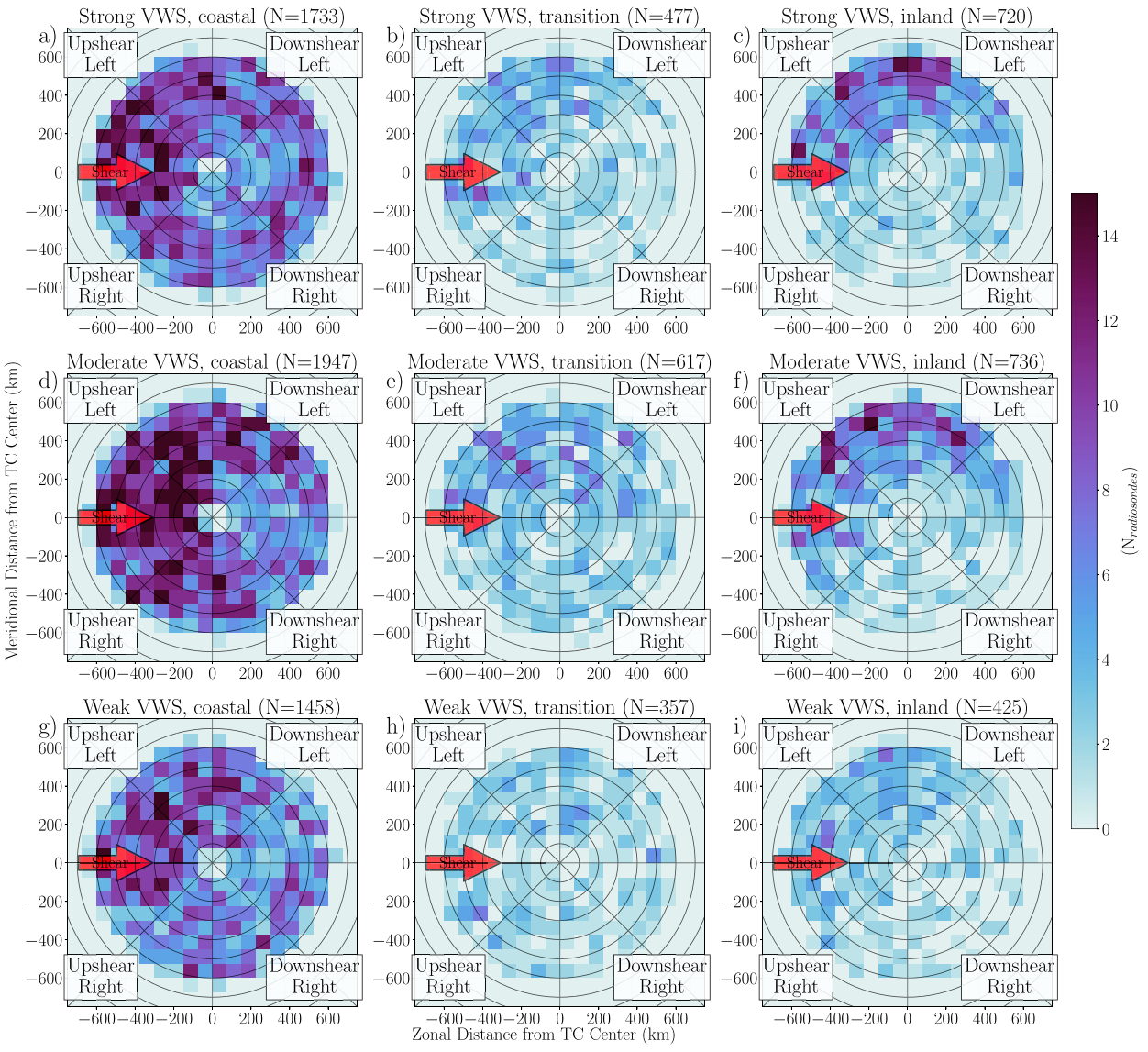

FIG. 2. Plan view plot of radiosonde location ($N_{\text{radiosondes}}$; shaded squares) for (a)–(c) strongly, (d)–(f) moderately, and (g)–(i) weakly sheared TCs in (left) coastal, (center) transition, and (right) inland environments using a VWS-relative reference frame. Radiosonde reports have been rotated around the TC center such that the VWS vector (red arrow) at the time of tornado occurrence is pointing to the right on the figure.

- Subtract the nondivergent and irrotational winds of the TC from the total wind at 850 and 200 hPa to obtain the ambient wind field;
- Average the resulting ambient wind field within a 500-km radius of the TC center at both isobaric levels, and compute their difference.

VWS data are separated into three categories based on the reanalysis-derived distribution for all Atlantic TCs from 1979 to 2019 (Rios-Berrios and Torn 2017; Ditchek et al. 2019): 1) strong (>11.2 m s^{-1}; upper 33rd percentile), 2) moderate (6.8–11.2 m s^{-1}; middle 33rd percentile), and 3) weak (<6.8 m s^{-1}; bottom 33rd percentile). Table 1 shows the distribution of TC tornadoes among the three VWS categories. Both North Atlantic TCs that produce tornadoes and, more generally, landfalling TCs occur more frequently in moderate-to-strong VWS compared to TCs in the rest of the North Atlantic (Corbosiero and Molinari 2002; Schenkel et al. 2020).

c. TC outer size data

TC outer size is computed to determine its potential contribution to differences among the various subsets of kinematic and thermodynamic convective-scale environments diagnosed from dropsondes and radiosondes. This study uses the radius at which the azimuthal-mean 925-hPa azimuthal wind equals 6 m s^{-1} (r_6), computed from ERA-5 reanalysis data, as a TC outer size metric (Schenkel et al. 2017; Bian et al. 2021).

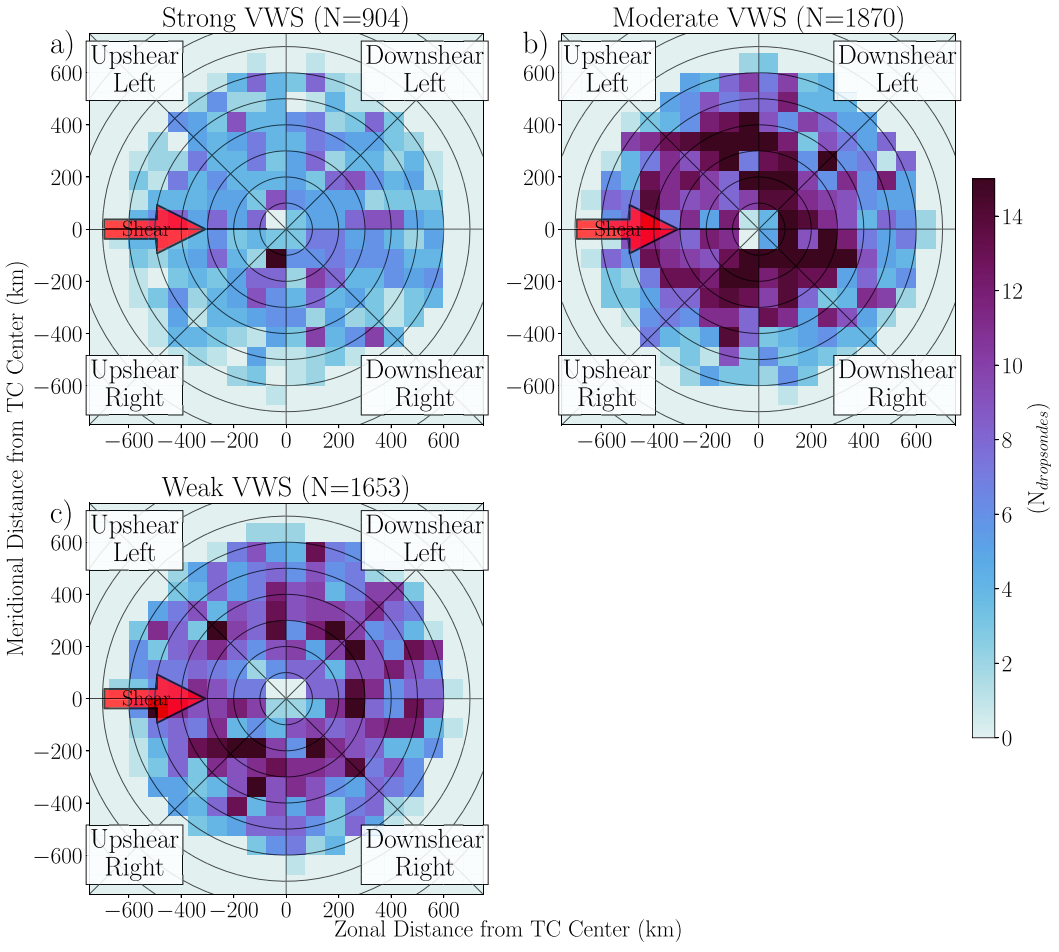

FIG. 3. Plan view plot of dropsonde locations ($N_{\text{radiosondes}}$; shaded squares) for TCs in (a) strong, (b) moderate, and (c) weak VWS in a VWS-relative reference frame. Dropsondes have been rotated around the TC center such that the VWS vector (red arrow) at the time of tornado occurrence is pointing to the right on the figure.

This prior work has also shown that reanalysis TC outer size is well-represented (Schenkel et al. 2017; Bian et al. 2021). We calculate r_6 similar to prior work (Chavas and Vigh 2014; Schenkel et al. 2018): 1) interpolate 925-hPa reanalysis winds to a TC-centered polar grid, 2) remove the ambient wind from the total wind, which is calculated using the same method used as the ambient winds for VWS (Davis et al. 2008), 3) calculate the azimuthal-mean of the azimuthal wind, 4) spatially interpolate the wind field to a grid spacing of 12.5 km (i.e., 0.5 times ERA-5 output grid spacing), and 5) extract r_6 as the first grid point outside the radius of maximum wind where the azimuthal-mean azimuthal wind equals 6 m s^{-1}. We use a reanalysis-derived TC outer size metric instead of IBTrACS data for three reasons. First, IBTrACS metrics are defined at 10 m above the surface and, hence, are subject to surface friction-induced decreases as the TC approaches land. However, the above-surface outer size of the TC wind field does not change until shortly after TC landfall, suggesting that a metric near the boundary layer top better quantifies TC outer size evolution (Chen and Chavas 2020). Second, IBTrACS TC outer wind field size metrics are subjectively derived without any postseason analysis until 2004. Last, outer size metrics are undefined for TCs with intensities < 34 kt (1 kt $\approx$ 0.51 m s^{-1}) since these metrics include the radius of 34-, 50-, and 64-kt winds (Landsea and Franklin 2013; Knaff et al. 2014).

d. *Defining coastal versus inland environments*

We use the Global Self-consistent, Hierarchical, High-resolution Geography (GSHHG) Database at a horizontal grid spacing of ~1 km (Wessel and Smith 1996) to calculate the distance of tornadoes and radiosondes from the coast. We then define three regimes using the distribution of tornado distance from the coast: 1) coastal (<23 km; bottom 33rd percentile), 2) transition (23–125 km; middle 33rd percentile), and 3) inland (>125 km; upper 33rd percentile) environments. In addition to classifying the TC tornadoes, these distance thresholds will also be applied to radiosonde data along with using dropsondes as part of a fourth regime—the ocean. This additional category is necessitated by supercells frequently intensifying upon reaching the coast (Baker et al. 2009; Eastin and Link 2009).

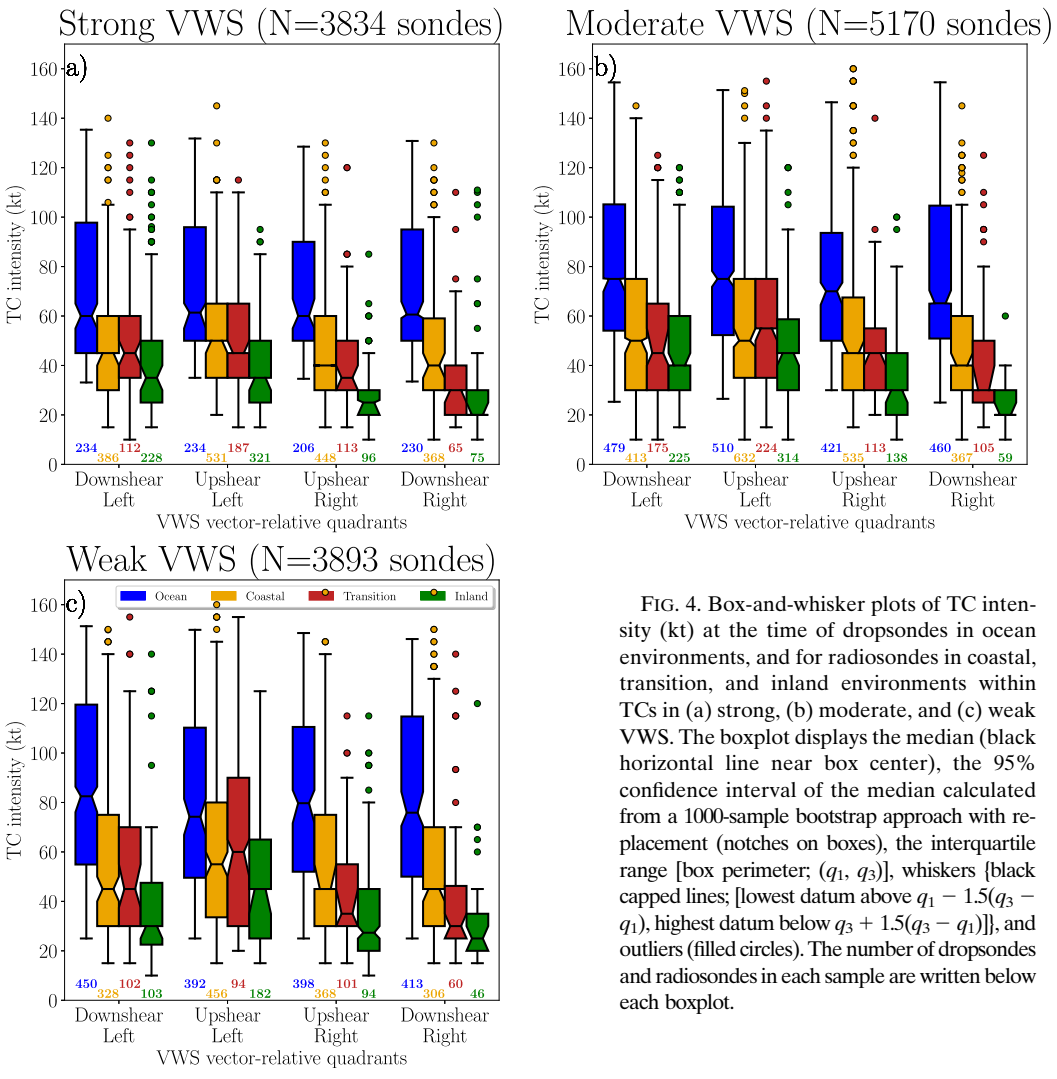

FIG. 4. Box-and-whisker plots of TC intensity (kt) at the time of dropsondes in ocean environments, and for radiosondes in coastal, transition, and inland environments within TCs in (a) strong, (b) moderate, and (c) weak VWS. The boxplot displays the median (black horizontal line near box center), the 95% confidence interval of the median calculated from a 1000-sample bootstrap approach with replacement (notches on boxes), the interquartile range [box perimeter; (q_1, q_3)], whiskers {black capped lines; [lowest datum above $q_1 - 1.5(q_3 - q_1)$, highest datum below $q_3 + 1.5(q_3 - q_1)$]}, and outliers (filled circles). The number of dropsondes and radiosondes in each sample are written below each boxplot.

e. Radiosonde and dropsonde data

Radiosonde data from 1979 to 2019, obtained from the NOAA Integrated Global Radiosonde Archive (IGRA), version 2 (Durre et al. 2006), are used to examine the kinematic and thermodynamic environments of TCs over land. To compare with these land environments, GPS dropsonde data in TCs from 1996–2017 are obtained from NOAA aircraft reconnaissance and various field experiments detailed in Table 2. To maximize our sample size, we include radiosondes from the CONUS, Canada, Central America, Bermuda, and the Caribbean. Dropsondes are taken from all over-water Atlantic TCs. Both the radiosonde and dropsonde data are quality controlled using several physical and internal consistency checks from NOAA and the NCAR Earth Observing Laboratory (EOL), respectively. Additionally, guidelines from prior work are used to ensure sufficient vertical data density and that each sonde is not too close to the TC center (i.e., ≥75-km radius from TC center; Molinari and Vollaro 2008, 2010). The latter condition precludes examining the convective-scale environments associated with the TC inner-core tornado maxima (McCaul 1991; Schultz and Cecil 2009). Moreover, each dropsonde must have been released at an altitude of at least 8 km to be included in our analysis, since the cell motion algorithm requires data from the surface to 8 km (Bunkers et al. 2000, 2014). The first 30 s of temperature and relative humidity data from each dropsonde are also removed to allow the thermistor to equilibrate to its environment (Bogner et al. 2000; Molinari and Vollaro 2010). Finally, we consider only those dropsondes and radiosondes located between 75 and 615 km from the TC center to match the distance over which 95% of tornadoes occur (Novlan and Gray 1974; McCaul 1991). This also ensures a similar distribution of sonde distances among each combination of coastal and VWS subsets examined. Together, these criteria yield 8470 radiosondes in 406 TCs and 4427 dropsondes in 94 TCs as shown in Tables 3 and 4 . The location of each radiosonde stratified by both coastal and VWS regime are shown in Fig. 2,

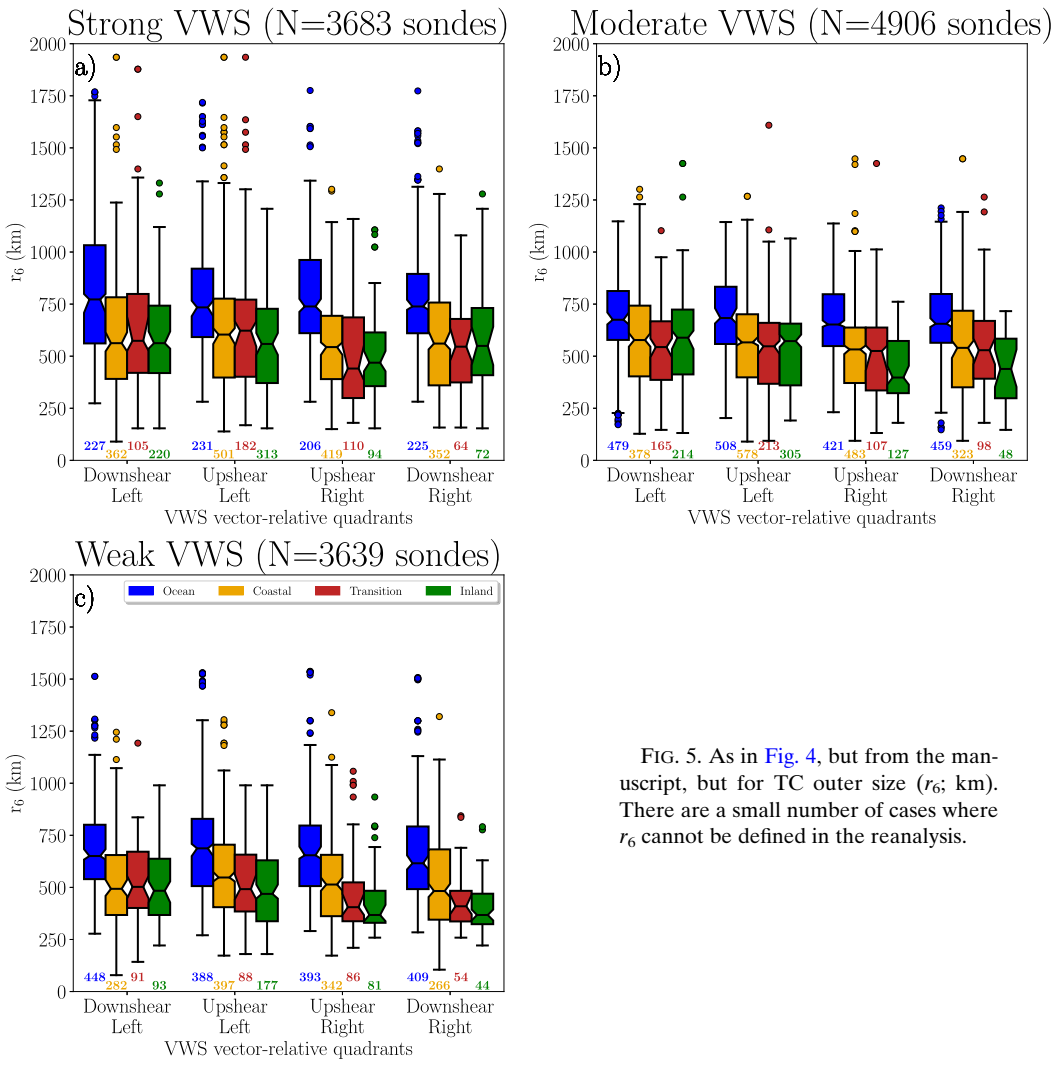

FIG. 5. As in Fig. 4, but from the manuscript, but for TC outer size (r_6; km). There are a small number of cases where r_6 cannot be defined in the reanalysis.

while similar plots are shown for dropsondes for each VWS regime in Fig. 3. Figures 2 and 3 show that the radiosondes and dropsondes are largely sampling TC outer winds (i.e., radius > 200 km from TC center) as shown by their median distance from the TC center of 383 and 449 km for dropsondes and radiosondes, respectively. Coincidentally, median TC tornado distance is slightly inward of these radii (i.e., 320 km; Schultz and Cecil 2009; Edwards 2012).

Figures 4 and 5 also show TC intensity and outer size differences among the various coastal and VWS regimes that typically characterized by: 1) decreases in TC intensity and, to a lesser extent, outer size in inland environments associated with greater TC–land interaction (Kaplan and DeMaria 1995; Chen and Chavas 2020), 2) stronger and smaller TCs in weak VWS (DeMaria and Kaplan 1994; Rios-Berrios and Torn 2017), and 3) weaker and, to a lesser extent, smaller TCs in the right-of-VWS vector quadrants (i.e., typically southern half of TC; Corbosiero and Molinari 2003; Schenkel et al. 2020). The sensitivity of our analysis to these disparities are partially quantified in the results section through further subsetting of the data to examine those TCs with similar TC intensity and outer size (i.e., Figs. 12 and Figs. S1 and S2 in the online supplemental material). Despite these efforts, some of these subset sample sizes are limited and, hence, may be associated with nontrivial uncertainty due to the diverse structural characteristics of the TCs being sampled and smaller sample sizes inherent to certain subsets—especially in the transition and inland environments.

As in prior work (Molinari and Vollaro 2008; Edwards and Thompson 2012), these dropsondes and radiosondes do not necessarily represent tornado proximity soundings, rather these data provide a bulk statistical assessment of how kinematic and thermodynamic environments in TCs change in response to VWS and coastal distance. Hence, the soundings in this study may be less favorable than those from tornado proximity soundings in prior work (McCaul 1991; Edwards and Thompson 2012). Sonde data are used to quantify kinematic favorability of convective-scale environments for TC tornadoes using both 0–3-km and 0–1-km convective cell-relative helicity, composite median hodographs, plan view plots of the

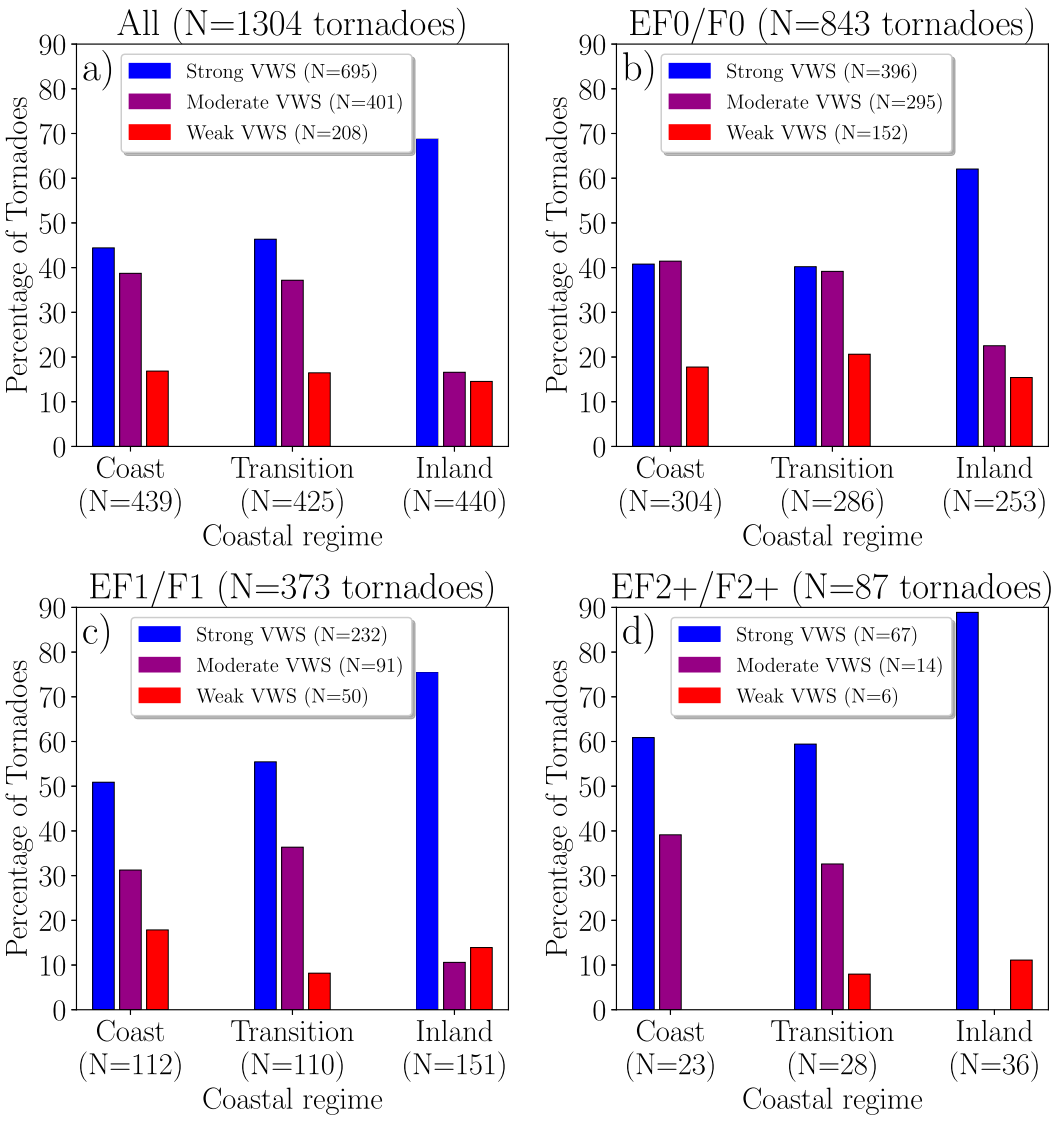

FIG. 6. Bar plots of TC tornado occurrence (percentage) stratified by the nine combinations of VWS and coastal regimes for (a) all tornadoes, (b) EF0/F0 tornado damage, (c) EF1/F1 tornado damage, and (d) EF2+/F2+ tornado damage. Each bar plot is expressed as the percentage of the number of tornadoes for a given VWS category within a given tornado damage category and coastal regime. The sample sizes along the *x* axis show the total number of tornadoes in a given coastal regime within a given tornado damage category, while the legend contains the number of tornadoes for each VWS category within each tornado damage bin. There is one tornado in the TCTOR archive classified with an undefined damage rating.

total, TC, and ambient wind vectors, and lower-tropospheric vertical profiles of TC-relative tangential and radial winds (Molinari and Vollaro 2008, 2010). Convective cell motion for the helicity calculations is estimated using the methodology of Bunkers et al. (2000) with the modifications suggested by Ramsay and Doswell (2005) and Bunkers et al. (2014). This assumes that cell motion is equal to the sum of the 0–8-km pressure-weighted mean wind (Bunkers et al. 2014), with the addition of a component with a magnitude of 7.5 m s^{-1} rotated 90° clockwise relative to the 0–6-km vertical wind shear (Ramsay and Doswell 2005). The cyclonic advection of the sondes by the TC tangential winds adds a component associated with the horizontal variations in the curvature of the wind. This contribution may artificially enhance the helicity measured by the sonde by 5%–8% (Molinari and Vollaro 2010), especially those sondes closer to the TC center, motivating the removal of sondes within 75 km of the storm. This artificial enhancement of sonde helicity is retained in our data, similar to prior work (McCaul 1991; Baker et al. 2009) since its removal requires geolocation at each vertical level, which is unavailable in the radiosondes and some dropsondes.

To quantify convective-scale thermodynamic environmental favorability, our study uses 0–3-km CAPE, using a 200-m mixed layer (Romps and Kuang 2011; Molinari et al. 2012), and composite median skew T–log$p$ diagrams. Last, to account for differences in radiosonde launch altitudes, all data are transformed into the vertical coordinate of Gal-Chen and Somerville (1975) using a vertical grid spacing of 50 m (Parker 2014):

$$z^* = H\frac{z - z_{\text{sfc}}}{H - z_{\text{sfc}}}, \tag{1}$$

where H is the approximate height of the tropopause assumed to be 12 km and z_{sfc} is the sonde surface altitude computed relative to mean sea level. Lower-tropospheric metrics are used given that tornadic supercells in TCs are shallower (Spratt et al. 1997; McCaul and Weisman 1996), and favorable environmental conditions are typically located within the lower troposphere (McCaul 1991; Molinari and Vollaro 2008). Statistical differences between median kinematic and thermodynamic characteristics of convective-scale environments as a function of VWS and the coastal regime are evaluated using the 1000-sample bootstrap resampling approach, with replacement, according to a two-tailed test.

3. Analysis and results

This analysis first examines how tornado frequency and location change as a function of both VWS and distance from the coast. We then use radiosondes and dropsondes to examine convective-scale environments to provide a greater physical understanding of tornado occurrence. In the interest of brevity, portions of the sonde analysis will focus exclusively on strongly sheared TCs.

a. *VWS impact on tornado occurrence in coastal versus inland environments*

1) TORNADO FREQUENCY

Analysis of tornado frequency for each damage rating stratified by both VWS magnitude and coastal distance regime (Fig. 6) shows that strongly sheared TCs produce the most tornadoes, including those associated with the most damage (i.e., EF2+/F2+), in all three coastal regimes. Specifically, strongly sheared TCs produce 44% and 46% of tornadoes in coastal and transition regimes, respectively, and 69% of inland tornadoes. Strongly sheared TCs also produce the largest percentage of EF2+/F2+ tornadoes in coastal (61%), transition (59%), and inland (89%) environments. Of any combination of coastal and VWS regimes, EF2+/F2+ tornadoes occur most frequently in inland environments within strongly sheared TCs (Fig. 6a).

Next, Fig. 7 shows in greater detail that TC tornadoes more frequently occur in strong VWS as their distance from the coast increases. In particular, the VWS distribution (i.e., box-and-whiskers plot) for inland tornadoes shifts toward larger values and narrows, as shown by median VWS in inland environments (12.8 m s^{-1}) that is statistically stronger at the 95% confidence interval compared to coastal tornadoes (10.6 m s^{-1}). Beyond a 200-km distance of the tornado from the coastline, VWS does not statistically change. This may suggest that VWS in this range is strong enough to favor tornado occurrence, while being weak enough such that TCs do not dissipate too quickly (Paterson et al. 2005; Schenkel et al. 2020).

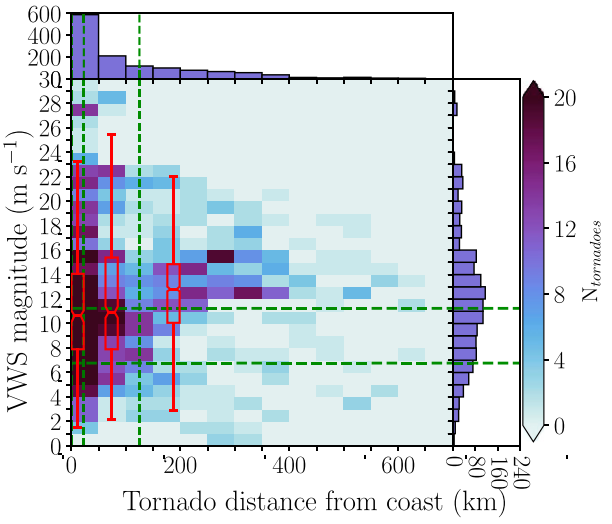

FIG. 7. Joint histogram of tornado distance from the coast (km) vs VWS magnitude (m s^{-1}) at the time of tornado occurrence. The one-dimensional histograms on top and to the right show tornado distance from the coast and VWS magnitude, respectively. The dashed green vertical lines demarcate the boundaries between coastal, transition, and inland environments. The dashed green horizontal lines demarcate the boundaries between weak, moderate, and strong VWS. The boxplots (from left to right) represent the VWS distribution statistics for coastal, transition, and inland tornadoes. The boxplots display the median (red horizontal line near box center), the 95% confidence interval of the median calculated from a 1000-sample bootstrap approach with replacement (red notches on boxes), the interquartile range [red box perimeter; (q_1, q_3)], and whiskers {red-capped lines; [lowest datum above $q_1 - 1.5(q_3 - q_1)$, highest datum below $q_3 + 1.5(q_3 - q_1)$]} for coastal, transition, and inland environments.

Together, these results suggest that coastal tornadoes can occur in all VWS regimes with strongly sheared TCs producing the most cases, whereas inland tornadoes primarily occur in strongly sheared TCs. The enhanced sensitivity of inland tornado production to VWS may imply that inland environments are marginal for tornadoes without strong VWS, especially as the TC wind field weakens and the storm is located increasingly further from coastal baroclinic zones and warm, moist onshore flow (Kaplan and DeMaria 1995; Knupp et al. 2006). However, inland tornadoes are not completely absent in weakly or moderately sheared TCs, suggesting that VWS is not the sole factor determining inland tornado production.

2) TORNADO LOCATION

Map view plots of tornado location within strong (Fig. 8a), moderate (Fig. 8b), and weak (Fig. 8c) VWS show that tornadoes occur further inland for strongly sheared TCs throughout the CONUS. In particular, the median value of tornado distance from the coast is shifted statistically further inland at the 95% confidence interval for strongly sheared TCs (90 km) compared to moderately (35 km) and weakly (54 km) sheared TCs. Moreover, tornado latitude is typically further poleward

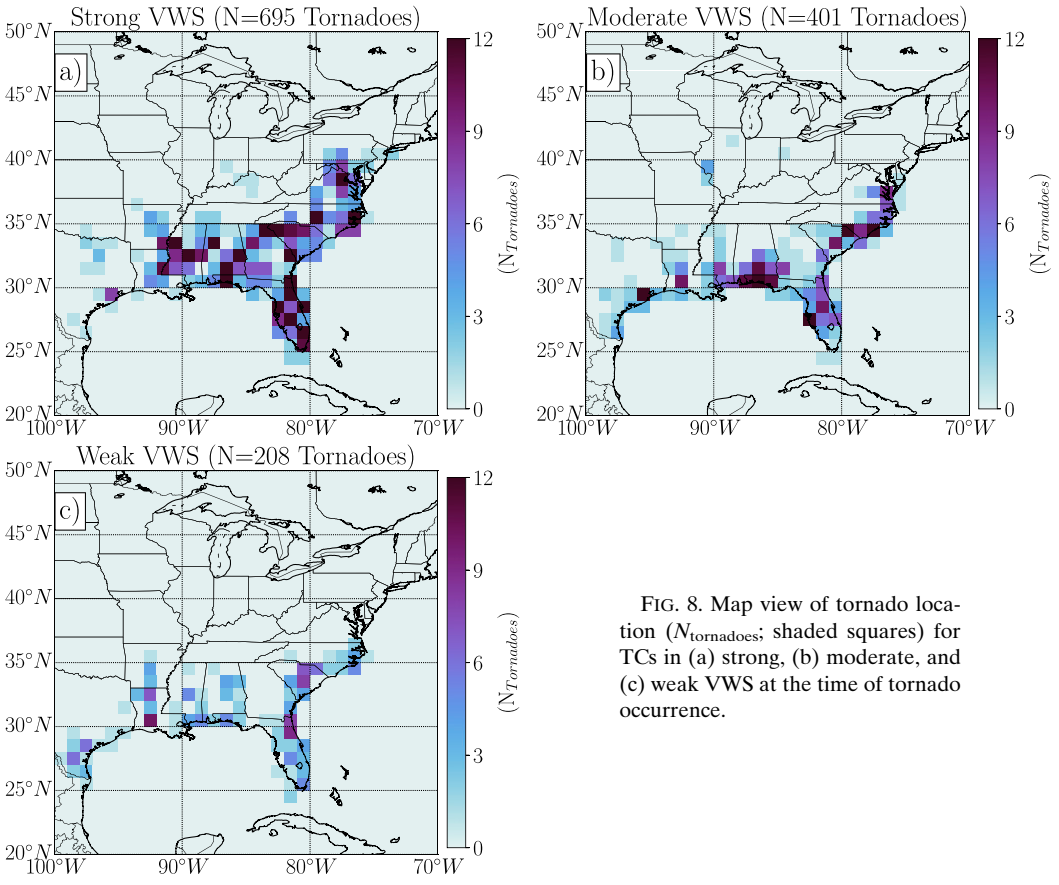

FIG. 8. Map view of tornado location ($N_{\text{tornadoes}}$; shaded squares) for TCs in (a) strong, (b) moderate, and (c) weak VWS at the time of tornado occurrence.

for TCs in strong VWS. Specifically, median latitude in strongly sheared TCs (32.8°N) is statistically further poleward, at the 95% confidence interval, compared to moderately (31.2°N) or weakly (30.9°N) sheared TCs.

Next, the cyclone-relative location of tornadoes plotted relative to the VWS vector direction (Fig. 9) shows that tornadoes most frequently occur in the downshear sector of the TC regardless of VWS magnitude or coastal location. More specifically, tornadoes in weakly sheared TCs show a distinctive shift to the downshear sector between coastal (77% of tornadoes) and inland environments (91%). In contrast, most tornadoes are located downshear in moderately and strongly sheared TCs (i.e., ≥88% in each subset) regardless of the coastal regime. The median VWS vector-relative angle of tornado occurrence statistically shifts clockwise, at the 95% confidence interval, into the downshear sector for inland tornadoes compared to the coast for strongly (13° further clockwise in inland compared to coast), moderately (9°), and weakly (26°) sheared TCs. Tornadoes also increasingly occur in the TC outer region in inland environments compared to coastal environments. For strongly sheared TCs, the inner-core downshear-left maxima of tornadoes weakens with increasing distance inland, such that 74% of tornadoes are concentrated in the downshear-right quadrant at radii greater than 200 km (i.e., TC outer region; Corbosiero and Molinari 2002; Schultz and Cecil 2009).

Next, Fig. 10 shows that tornado occurrence shifts to TC outer radii with increasing distance from the coastline in strongly, moderately, and weakly sheared TCs. In particular, tornadoes increasingly occur at radii ≥ 200 km in inland environments compared to coastal environments in strongly (73% of coastal versus 91% of inland tornadoes), moderately (68% versus 92%), and weakly sheared TCs (69% versus 88%). However, only moderately sheared TCs show tornado occurrence shifting statistically further from the TC center inland compared to coastal environments, with median values that are statistically different at the 95% confidence interval (260 km at coast versus 347 km inland). The absence of similar statistical changes for strongly sheared TCs may be due to the outer-region maximum in tornado occurrence that is present in all three coastal regimes.

Together, these results suggest that increases in distance from the coast are associated with tornadoes that are increasingly confined to: 1) the downshear sector (primarily downshear right in strongly sheared cases), 2) TC outer region (i.e., >200 km from TC center), and 3) more strongly sheared TCs. As such, the synoptic-scale environment of the TC is a key discriminant determining both whether and where inland tornadoes may occur, especially in inland environments (Edwards 2012; Schenkel et al. 2020). More broadly, these results may shed insight into the postlandfall convective evolution of TCs, suggesting that inner-core convection may weaken more quickly

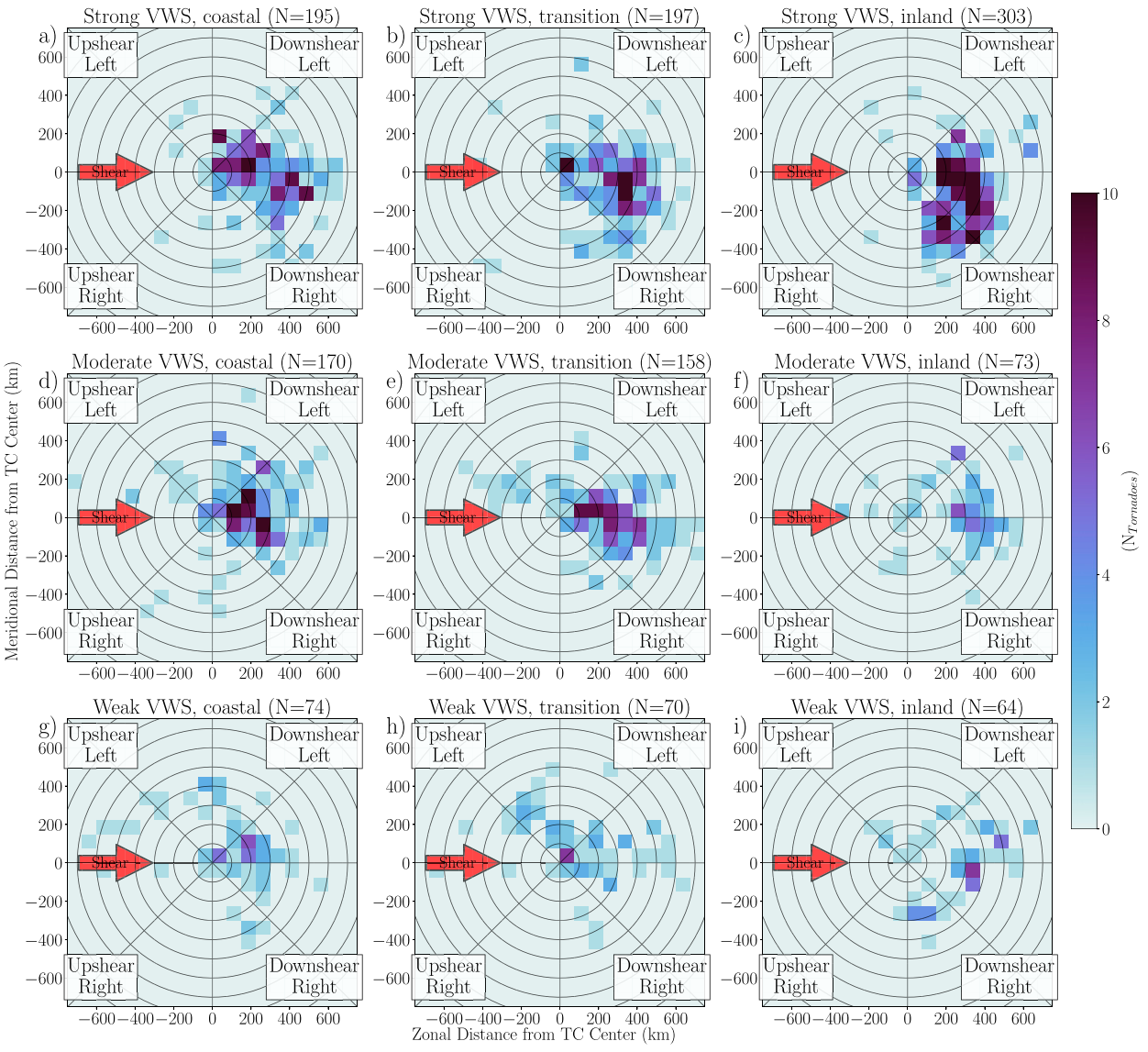

FIG. 9. Plan view plot of tornado location ($N_{\text{tornadoes}}$; shaded squares) in a VWS-relative reference frame for TCs in (a)–(c) strong, (d)–(f) moderate, and (g)–(i) weak VWS for tornadoes at the (left) coast, (center) transition, and (right) inland environments. Tornado reports have been rotated around the TC center such that the VWS vector (red arrow) at the time of tornado occurrence is pointing to the right.

than the outer-region convection—especially in strongly sheared cases. Next, the kinematic and thermodynamic structure of convective-scale environments is examined to provide a greater physical understanding of the relationships documented here.

b. Convective-scale environments

1) KINEMATIC IMPACTS

Box-and-whisker plots of 0–3-km convective cell-relative helicity (Fig. 11) show the diversity in kinematic environments among the ocean and inland subsets within each VWS regime. As expected from the tornado analysis, the downshear-right quadrant of strongly sheared TCs is the only quadrant in which: 1) median helicity is approximately within the range associated with tornadic supercells (i.e., 100–260 $m^2 s^{-2}$; McCaul and Weisman 1996; McCaul et al. 2004) except in coastal environments and 2) helicity is larger with greater distance inland such that median helicity in inland environments is approximately double the coastal values. Indeed, these differences between the coastal and inland environments are sufficiently large to be statistically different at the 95% confidence interval. These increases in helicity with greater coastal distance occur despite statistical decreases in TC intensity, at the 95% confidence interval, between the coast (median intensity of 40 kt) and inland environments (20 kt; Fig. 4). However, the radiosondes largely sample the TC outer wind field, which does not

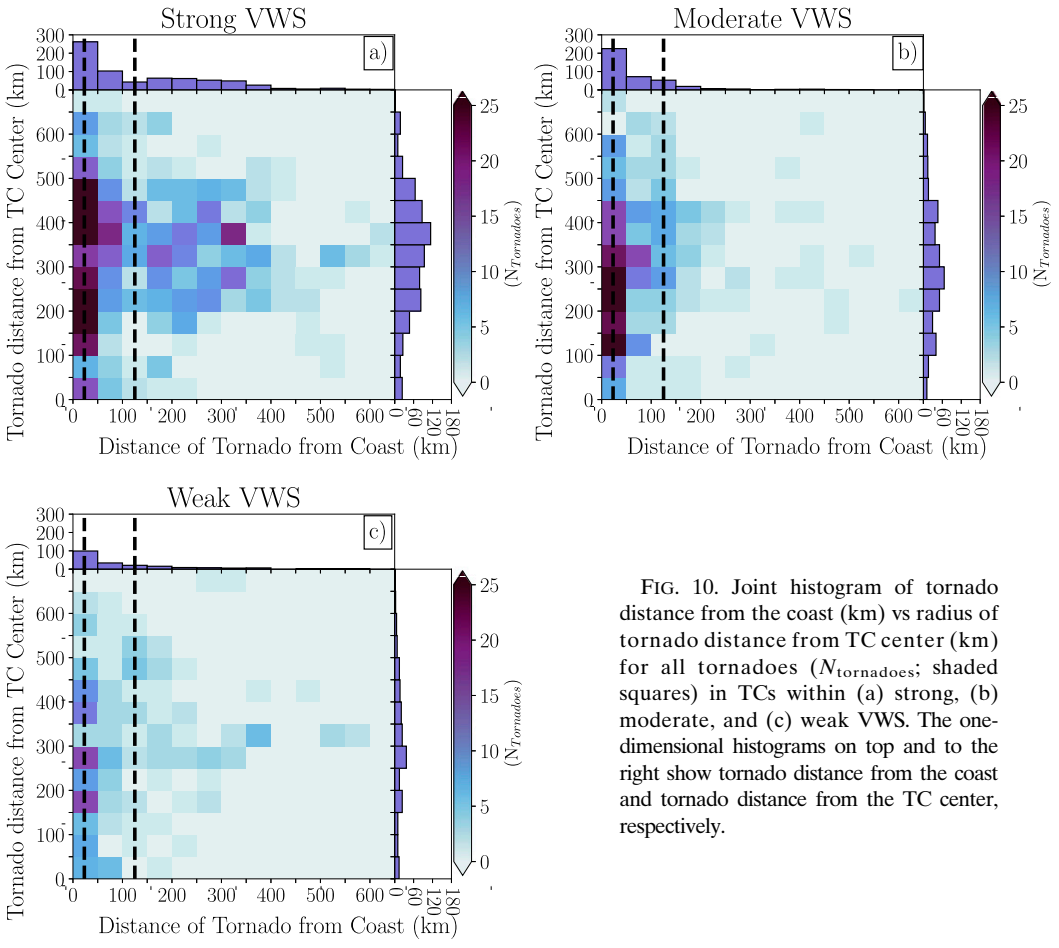

FIG. 10. Joint histogram of tornado distance from the coast (km) vs radius of tornado distance from TC center (km) for all tornadoes ($N_{\text{tornadoes}}$; shaded squares) in TCs within (a) strong, (b) moderate, and (c) weak VWS. The one-dimensional histograms on top and to the right show tornado distance from the coast and tornado distance from the TC center, respectively.

statistically change between the coast and inland environments, as shown by median r_6 of 561 versus 550 km for the two regimes, respectively. The absence of increases in either TC intensity or outer size may suggest that other factors are responsible for these helicity differences (e.g., stronger ambient winds). The downshear-left quadrant of strongly sheared TCs also is associated with enhanced helicity, although values are typically lower than the range associated with tornadic supercells (Schenkel et al. 2020) and do not increase with coastal distance. The two upshear quadrants of strongly sheared TCs show helicity that is also typically much smaller than the range of values associated with tornadic supercells, with no statistical changes in helicity between ocean to inland environments. Similarly, all quadrants in weakly and moderately sheared TCs are also generally unfavorable for tornadic supercells and show no systematic changes with increasing distance from the coast. While prior work suggested that helicity may increase inland for TCs (McCaul 1991), these results suggest that this only typically occurs for strongly sheared TCs. Additionally, while prior analyses of two case studies suggested that helicity is stronger at the coast compared to the ocean (Baker et al. 2009), these results suggest that there are generally no statistical differences in a large sample of cases, suggesting that surface friction-induced enhancements may be offset by smaller TC outer size and weaker TC intensity (Figs. 4 and 5).

We next show that increased 0–3-km convective cell-relative helicity is not a statistical artifact of VWS-induced differences in TC intensity and outer size among bins. This is shown by recreating Fig. 11 using only cases with TC intensity and outer size less than their respective median values computed for all TCs (i.e., intensity $<$ 50 kt, $r_6 <$ 566 km; Fig. 12). Indeed, corresponding plots of TC intensity (Fig. S1) and outer size (Fig. S2) for the subset of cases examined in Fig. 12 show smaller differences in TC intensity and no statistical change in outer size for a given VWS-relative quadrant between coastal and inland environments regardless of VWS. The conclusions from the subset of weaker and smaller TCs in Fig. 12 are qualitatively similar to those in Fig. 11. However, helicity is reduced in this subset of weaker and smaller TCs, especially in the ocean and coastal environments, suggesting that weak and/or small TCs typically do not produce tornadoes before and during landfall. Instead, only transition and inland regimes in the downshear-right quadrant of strongly sheared TCs are favorable for tornadoes (McCaul and Weisman 1996; McCaul et al. 2004). This favorability is associated with large increases in helicity with increasing distance from the ocean yielding

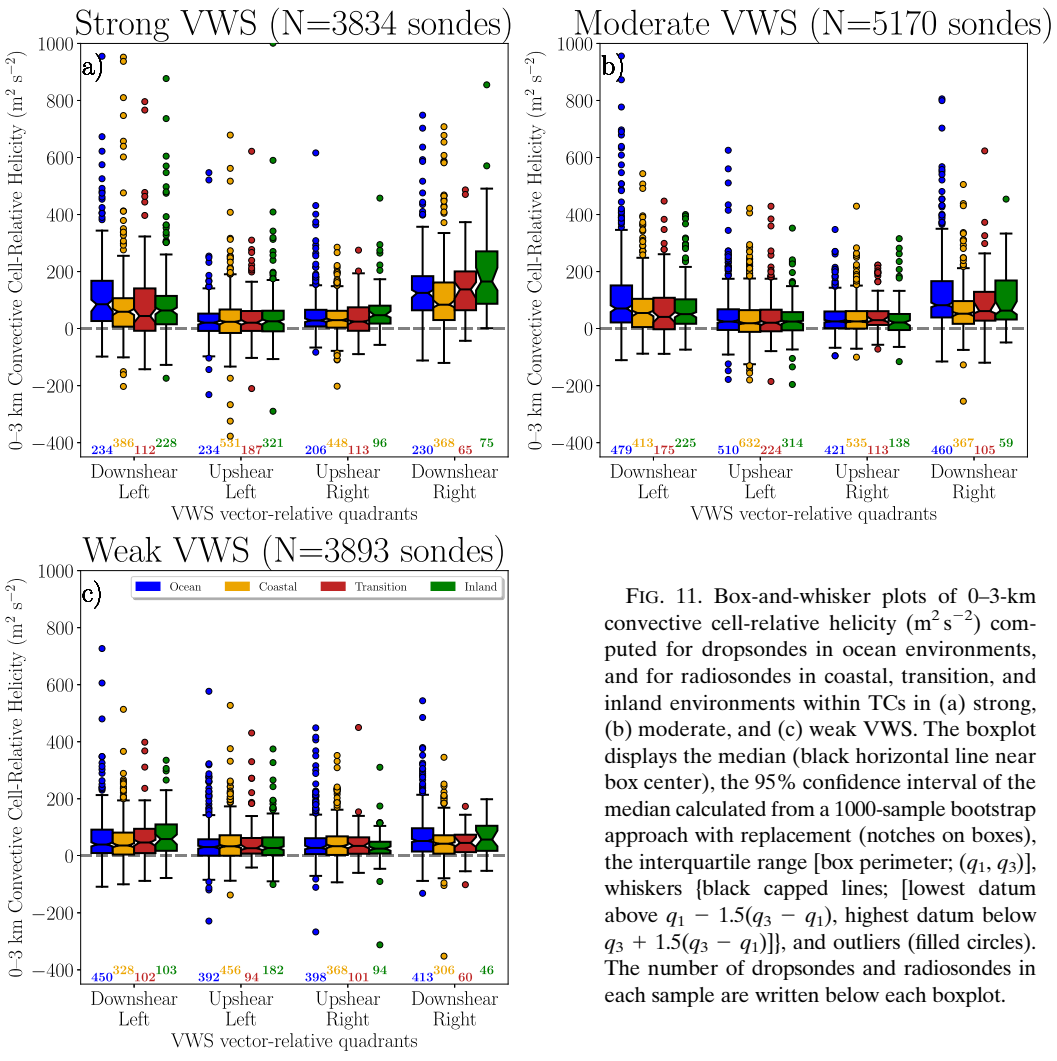

FIG. 11. Box-and-whisker plots of 0–3-km convective cell-relative helicity ($m^2 s^{-2}$) computed for dropsondes in ocean environments, and for radiosondes in coastal, transition, and inland environments within TCs in (a) strong, (b) moderate, and (c) weak VWS. The boxplot displays the median (black horizontal line near box center), the 95% confidence interval of the median calculated from a 1000-sample bootstrap approach with replacement (notches on boxes), the interquartile range [box perimeter; (q_1, q_3)], whiskers {black capped lines; [lowest datum above $q_1 - 1.5(q_3 - q_1)$, highest datum below $q_3 + 1.5(q_3 - q_1)$]}, and outliers (filled circles). The number of dropsondes and radiosondes in each sample are written below each boxplot.

median values in inland environments that are ~2.5 times larger than coastal environments. These differences are statistically different at the 95% confidence interval. Rather than being statistical artifacts, these results may suggest that tornado production at the coast is typically favored in more intense and/or larger TCs in strong VWS in the downshear-right quadrant. In contrast, inland tornado production is favored in a broader subset of TC intensities and outer sizes in strong VWS potentially in association with stronger lower-tropospheric ambient helicity, which will be shown later.

Next, box-and-whisker plots of 0–1-km convective cell-relative helicity for all sondes (Fig. 13) show additional insight into the vertical structure of kinematic environments in TCs. These results match those for the 0–3-km layer (Fig. 11), including that the downshear-right quadrant of strongly sheared TCs is the only quadrant typically favorable for tornadic supercells within all coastal regimes. Specifically, median 0–1-km helicity falls within the range of values associated with tornadic supercells (i.e., 33–210 $m^2 s^{-2}$; Thompson et al. 2003; Rasmussen 2003) and becomes statistically larger with greater distance inland. However, median helicity in oceanic and coastal environments is statistically lower, at the 95% confidence interval, compared to previously reported thresholds based on tornado proximity soundings (i.e., 98–463 $m^2 s^{-2}$; Eastin and Link 2009; Edwards et al. 2012), although these differences may be due to this study using all soundings regardless of their proximity to tornadoes. Inland environments in the downshear-right quadrant of strongly sheared TCs are even characterized by statistically stronger helicity at the 95% confidence interval than their oceanic counterparts potentially due to increased surface friction (Novlan and Gray 1974; Gentry 1983). Helicity is also more strongly concentrated near the surface with increasing distance from the coast, which is consistent with environments that are more favorable for tornadic supercells (Markowski et al. 2003; Thompson et al. 2003). Specifically, the 0–1-km layer constitutes 78% and 75% of 0–3-km helicity in inland and transition environments within the downshear-right quadrant, respectively, compared to 68% and 65% in the ocean and coastal environments. In contrast, the remaining quadrants and combinations of VWS and coastal regimes are generally not favorable for tornadic supercells.

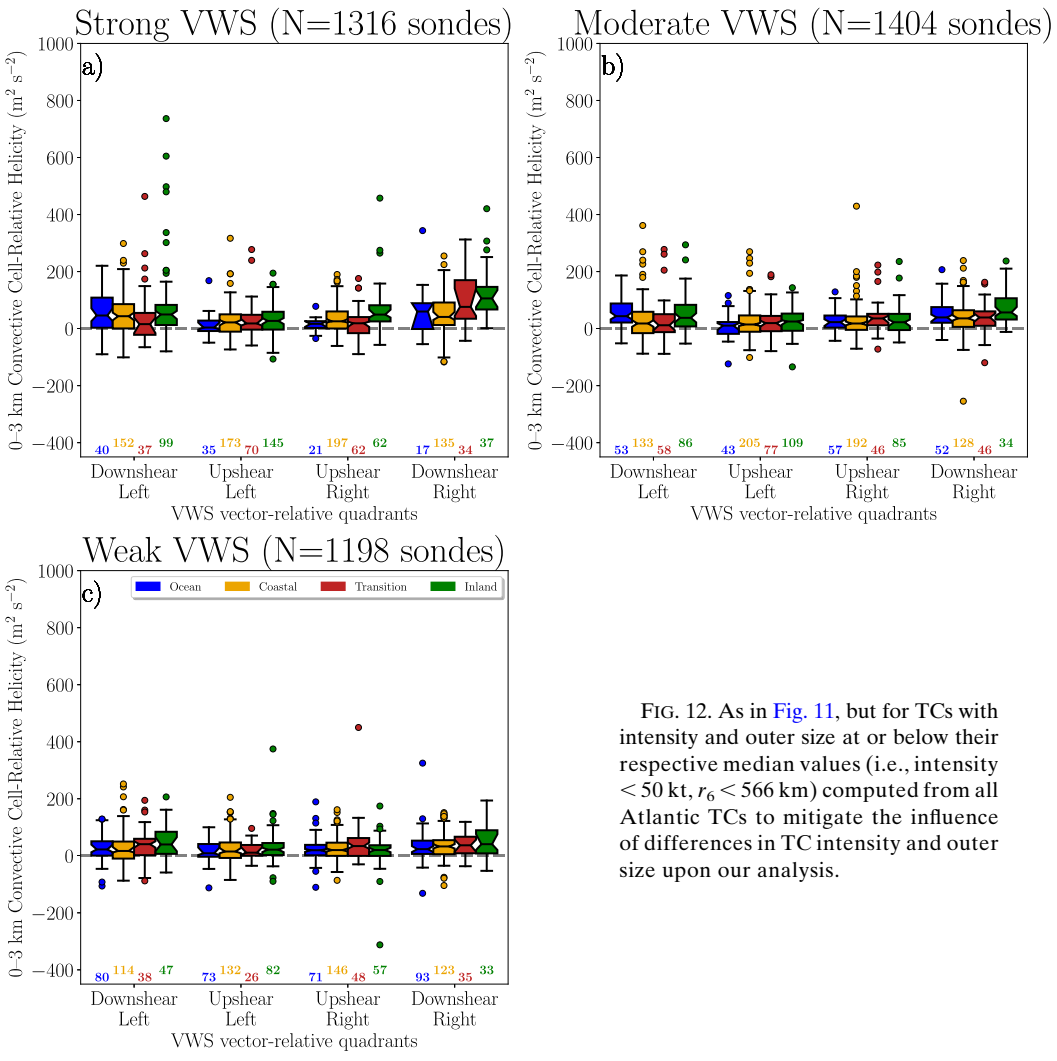

FIG. 12. As in Fig. 11, but for TCs with intensity and outer size at or below their respective median values (i.e., intensity < 50 kt, $r_6 < 566$ km) computed from all Atlantic TCs to mitigate the influence of differences in TC intensity and outer size upon our analysis.

From here on, the analysis of convective-scale kinematic environments will focus on strongly sheared TCs in the interest of brevity. Composite median hodographs, with TC motion removed, show that the coastal hodographs are located closer to the hodograph center compared to the ocean (Fig. 14) due to two factors. The first is stronger surface friction over land, yielding increased speed shear in the lowest 1 km. The second factor is weaker TC intensity and smaller outer size in the coastal subset compared to the ocean, which are both statistically different between these subsets at the 95% confidence interval (Figs. 4 and 5; Novlan and Gray 1974; Chen and Chavas 2020). An intercomparison of coastal, transition, and inland environments shows that, except for the near surface, the hodograph winds are not statistically different in the downshear-right quadrant, which is more consistent with the evolution of TC outer size (Fig. 5) rather than TC intensity (Fig. 4). Indeed, the radiosondes are primarily sampling TC outer winds, which are typically agnostic to inner-core wind changes (Merrill 1984; Chavas and Emanuel 2010). With the exception of the upshear-right quadrant, the remaining inland hodographs also do not show statistical differences in winds throughout the troposphere compared to coastal environments.

To understand the contribution of ambient versus TC winds in Fig. 14, we next show hodographs for the reanalysis-derived ambient winds for strongly sheared TCs, coincident with the time of the dropsondes and radiosondes (Fig. 15). Comparing ocean versus land environments, ambient winds show decreased near-surface wind speed due to friction, and a statistically stronger westerly component at the 95% confidence interval throughout the troposphere that imparts a stronger eastward component of TC motion. Indeed, composites of median zonal and meridional TC translation velocity for strongly sheared TCs at the time of radiosonde and dropsonde sampling (Fig. 16) show that sondes located farther from the coast are typically associated with stronger eastward TC motion. The differences in TC zonal motion between oceanic and inland environments in all four quadrants are upward of 3.5 m s^{-1}, which is statistically different at the 95% confidence interval. This stronger eastward motion is likely due to the TC being closer to

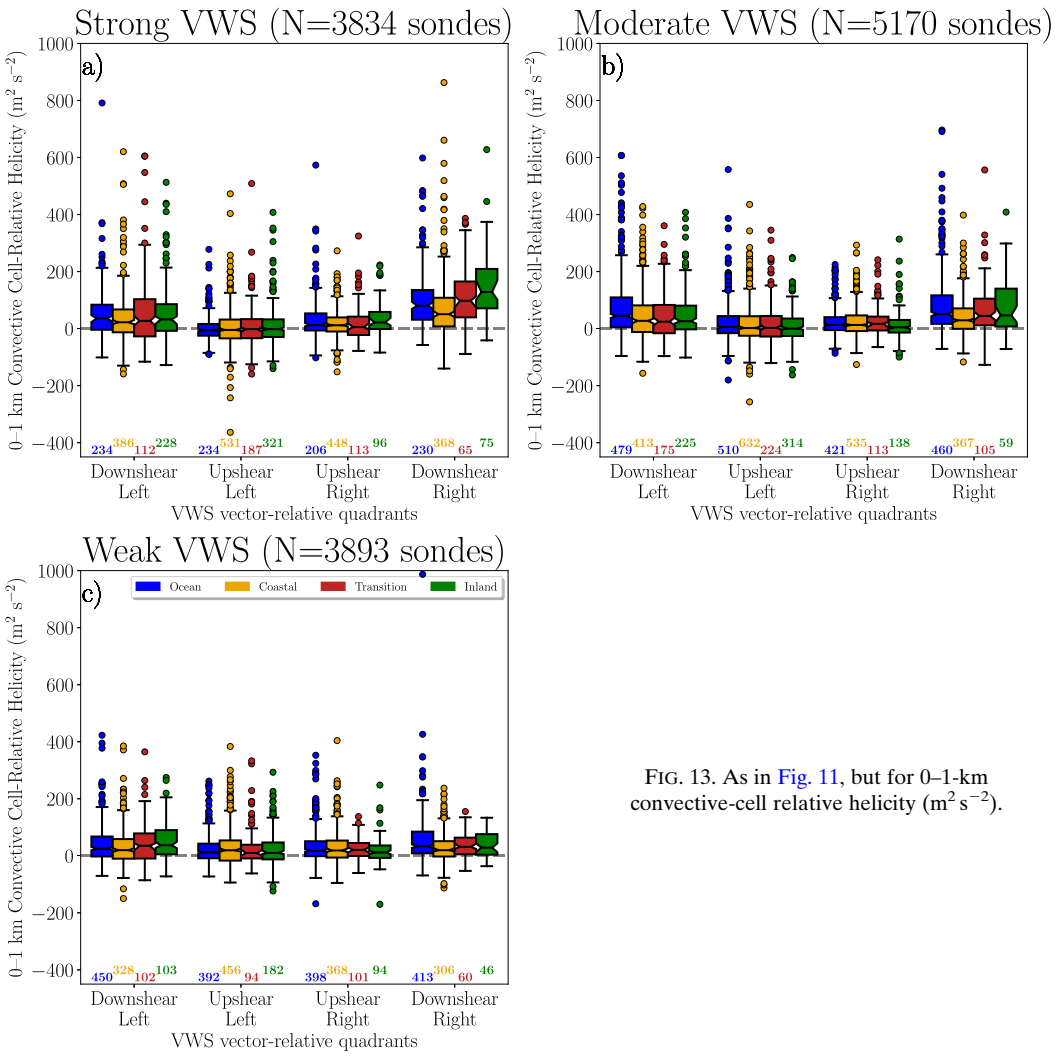

FIG. 13. As in Fig. 11, but for 0–1-km convective-cell relative helicity ($m^2 s^{-2}$).

the polar or subtropical jet when over land (Aiyyer and Thorncroft 2006; Verbout et al. 2007). Ambient hodographs also show that wind speed and directional shear are stronger with increasing distance inland, particularly within the mid-to-upper troposphere. These wind field changes with increasing distance inland are associated with increased 0–3-km convective cell-relative helicity in inland environments compared to either the ocean or coastal environments. In particular, the downshear-right quadrant shows median helicity of 46 $m^2 s^{-2}$ in inland environments that is statistically different at the 95% confidence interval compared to oceanic (20 $m^2 s^{-2}$) and coastal (28 $m^2 s^{-2}$) environments, respectively. While these increases in ambient helicity are not large enough to yield supportive environments for tornadoes by themselves (McCaul and Weisman 1996, 2001), their constructive superposition with the TC winds likely is given that helicity is a nonlinear product of the ambient and TC winds (Schenkel et al. 2020).

Partitioning of the ambient and TC winds in Fig. 17 suggests that several factors may contribute to enhanced median 0–3-km convective cell-relative helicity of the total wind within the downshear-right quadrant. Given that helicity is a nonlinear quantity, the median helicity of the total wind can be larger than the sum of the helicity from the TC and ambient winds if the two are strongly in phase (and vice versa). In the downshear-right quadrant, the median helicity associated with the TC winds is stronger in inland environments compared to the ocean or the coast, but not statistically different. However, the more strongly veering ambient winds constructively superimpose with the unchanged TC winds in the downshear-right quadrant of inland environments yielding helicity of the total wind field that is 1.5 and 2.0 times larger than either ocean or coastal environments, respectively. Indeed, these quantities are statistically different at the 95% confidence interval. Moreover, the helicity of the total wind field is more than double the helicity of the TC winds in inland environments, which suggests the importance of the ambient winds in creating favorable inland kinematic environments (Schenkel et al. 2020). In contrast to the downshear-right quadrant, the ambient and TC winds are sufficiently out of phase in the remaining

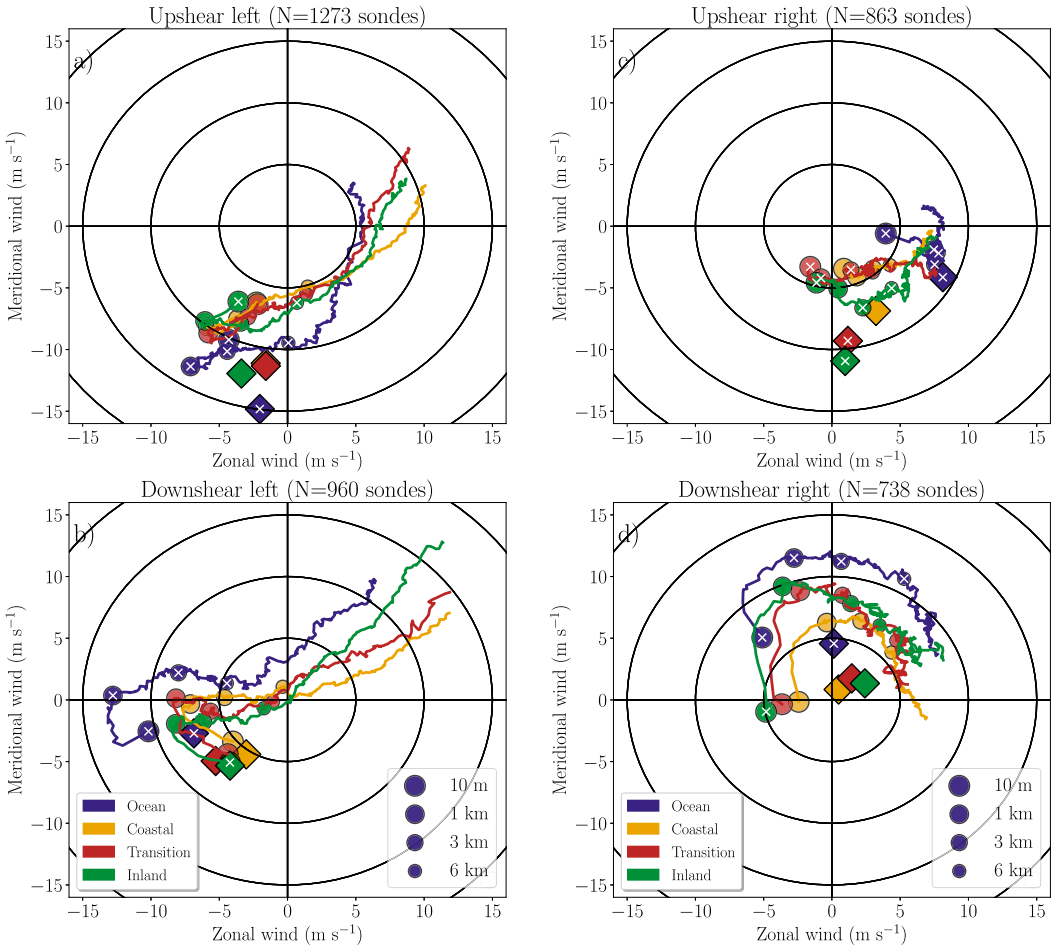

FIG. 14. Composite median hodograph for dropsondes and radiosondes, with TC motion removed from each sonde, in strongly sheared TCs within ocean, coastal, transition, and inland environments in the (a) upshear-left, (b) downshear-left, (c) upshear-right, and (d) downshear-right quadrants. The median convective cell-relative motion is denoted by the diamonds. The white X marks denote points that are statistically different at the 95% from the corresponding value for the coastal subset. Circles denote the height of 10-m, 1-km, 3-km, and 6-km winds.

three VWS-relative quadrants in all land environments. This result is associated with both helicity of the total wind field that is not statistically greater than the helicity of the TC wind, and values below those associated with TC tornadic supercells (Schenkel et al. 2020).

Next, composited vertical profiles of the tangential and radial winds in strongly sheared TCs, with TC motion removed, are shown (Fig. 18) to decompose the wind field response into the primary and secondary circulation of the TC. All quadrants show that the tangential wind field is statistically weaker, at the 95% confidence interval, in coastal environments compared to oceanic environments as expected due to TC landfall and increased surface friction (Kaplan and DeMaria 1995; Chen and Chavas 2020). However, perhaps most importantly, the tangential wind of the downshear-right quadrant is slightly stronger in inland and transition environments above 1 km compared to the coast. This results in the transition and inland tangential winds *not* being statistically different from the ocean, which contrasts with the other VWS-relative quadrants. Finally, the radial winds are typically weaker or unchanged when comparing land versus ocean environments, or when intercomparing coastal, transition, and land environments in any of the quadrants.

Together, these results suggest that the downshear-right quadrant of strongly sheared TCs is most favorable for tornadoes primarily within stronger and/or larger TCs at the coast. However, environments further inland may be more supportive of tornadoes within a broader variety of weaker and smaller TCs in association with the strengthening of the lower-tropospheric ambient winds and its constructive superposition with the TC winds in the downshear-right quadrant (Onderlinde and Nolan 2016; Schenkel et al. 2020). Alternatively, strong VWS may enhance convective-scale vorticity and vertical vorticity fluxes by convection helping to sustain the lower-to-midtropospheric

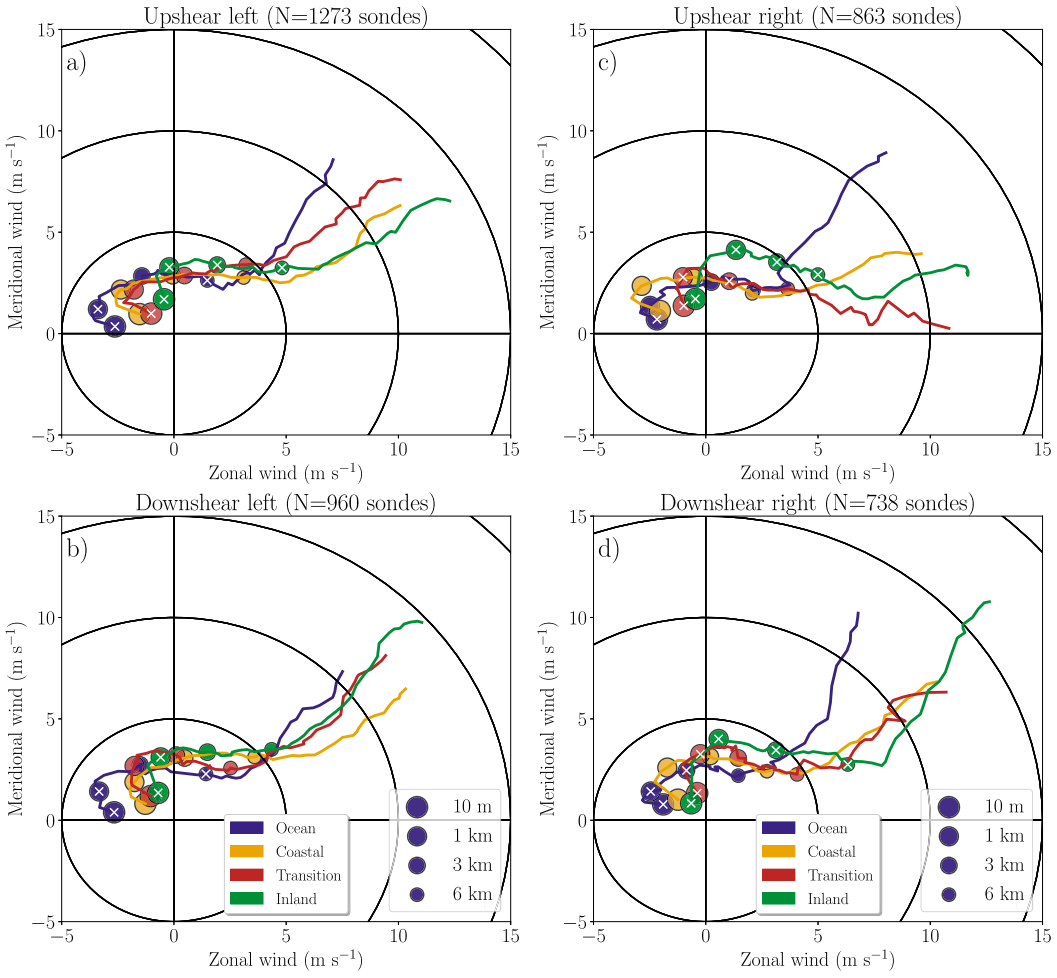

FIG. 15. Hodograph of ambient winds (m s^{-1}) at time of dropsonde and radiosonde occurrence at the ocean, coast, transition, and inland environments for strongly sheared TCs in the (a) upshear-left, (b) downshear-left, (c) upshear-right, and (d) downshear-right quadrants. Circles denote the height of the 10-m, 1-km, 3-km, and 6-km ambient winds, and the error bars denote the 95% confidence interval of the median values at each height.

tangential wind jet in the TC outer rainbands where most sondes in this study were located (Hence and Houze 2008; Didlake and Houze 2009).

These factors may help explain why tornado frequency and cyclone-relative location are different with increasing distance inland. However, nontrivial uncertainties exist in these results due to the small sample size and diverse subset of TCs examined particularly within inland environments, which warrants additional analysis. With an understanding of kinematic environments, the next section will focus on the changes in thermodynamic environments with greater distance inland.

2) THERMODYNAMIC IMPACTS

Box-and-whiskers plots of 0–3-km CAPE from dropsondes and radiosondes (Fig. 19) show that lower-tropospheric thermodynamic stability in the downshear-right quadrant is favorable for TC tornadoes in all combinations of VWS and coastal regimes (i.e., ~100–200 J kg^{-1}; Baker et al. 2009; Eastin and Link 2009) in contrast to the other three quadrants. Specifically, the downshear-right quadrant of strongly sheared TCs shows CAPE that statistically increases (at the 95% confidence interval) by 33% between the ocean and coast, while decreasing back to the range of its oceanic environments further inland. In contrast, although the remaining three VWS-relative quadrants in strongly sheared TCs also typically have sufficient lower-tropospheric CAPE in oceanic environments for tornadoes, values decrease as the distance from the coast increases to more marginal values for tornado production (McCaul 1991). In particular, the median CAPE for inland environments is 27%–44% of oceanic CAPE, which is statistically different at the 95% confidence interval. The decreases in CAPE away from the coast may explain why tornadoes are typically less frequent within inland environments in the downshear-left quadrant of strongly sheared TCs. Moderately sheared TCs are associated with smaller, yet statistically large, CAPE decreases in all quadrants except downshear right as the

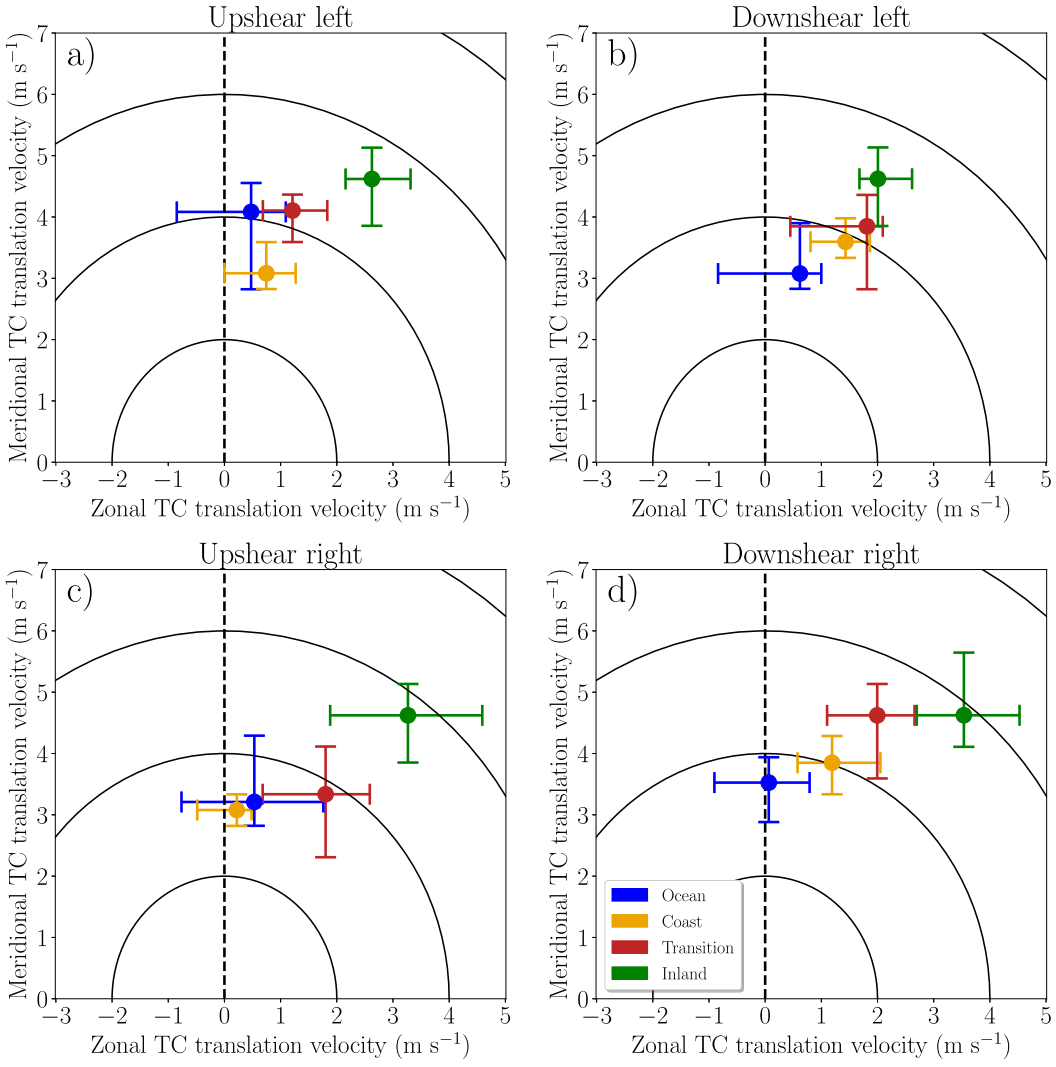

FIG. 16. Scatterplot of median zonal (m s^{-1}) vs meridional (m s^{-1}) TC translation velocity at the time of dropsonde and radiosonde occurrence at the ocean, coast, transition, and inland environments for strongly sheared TCs in the (a) upshear-left, (b) downshear-left, (c) upshear-right, and (d) downshear-right quadrants. Error bars denote the 95% confidence interval of the median zonal and meridional TC translation velocities. The black dashed line denotes the boundary between eastward and westward TC motion.

distance from the coast increases. Finally, weakly sheared TCs show marginal decreases in CAPE in all quadrants with distance from the coast such that CAPE generally remains favorable for inland tornadic supercells, especially in the downshear quadrants. Similar to the results for kinematic quantities, these results suggest that the variability in 0–3-km CAPE with coastal distance is dependent upon the VWS regime (McCaul 1991) for reasons to be discussed at the end of this section.

Composite median skew T–log$p$ diagrams (Fig. 20) in strongly sheared TCs show that inland environments are cooler and drier compared to the ocean. In the downshear-right quadrant, these temperature changes are larger and over a greater depth (i.e., lower troposphere) compared to the dewpoint differences (i.e., boundary layer), which results in the lower troposphere being slightly closer to saturation especially above the boundary layer. In particular, the strongest statistical differences (at the 95% confidence interval) are located within the first 3 km of the surface, with a maximum decrease in temperature of −2.8°C and reduction in dewpoint of −2.4°C. Compared to the downshear-right quadrant, the three remaining VWS-relative quadrants show decreasing temperature and dewpoint throughout the *entire* troposphere with increasing distance inland, with the largest cooling occurring between oceanic to coastal environments. Median values of surface temperature changes are approximately −(5.0–3.7)°C, while median dewpoint changes are maximized in the midtroposphere (≤−10.6°C) between oceanic to inland environments especially in the upshear half of the TC in the latter case. Both of these sets

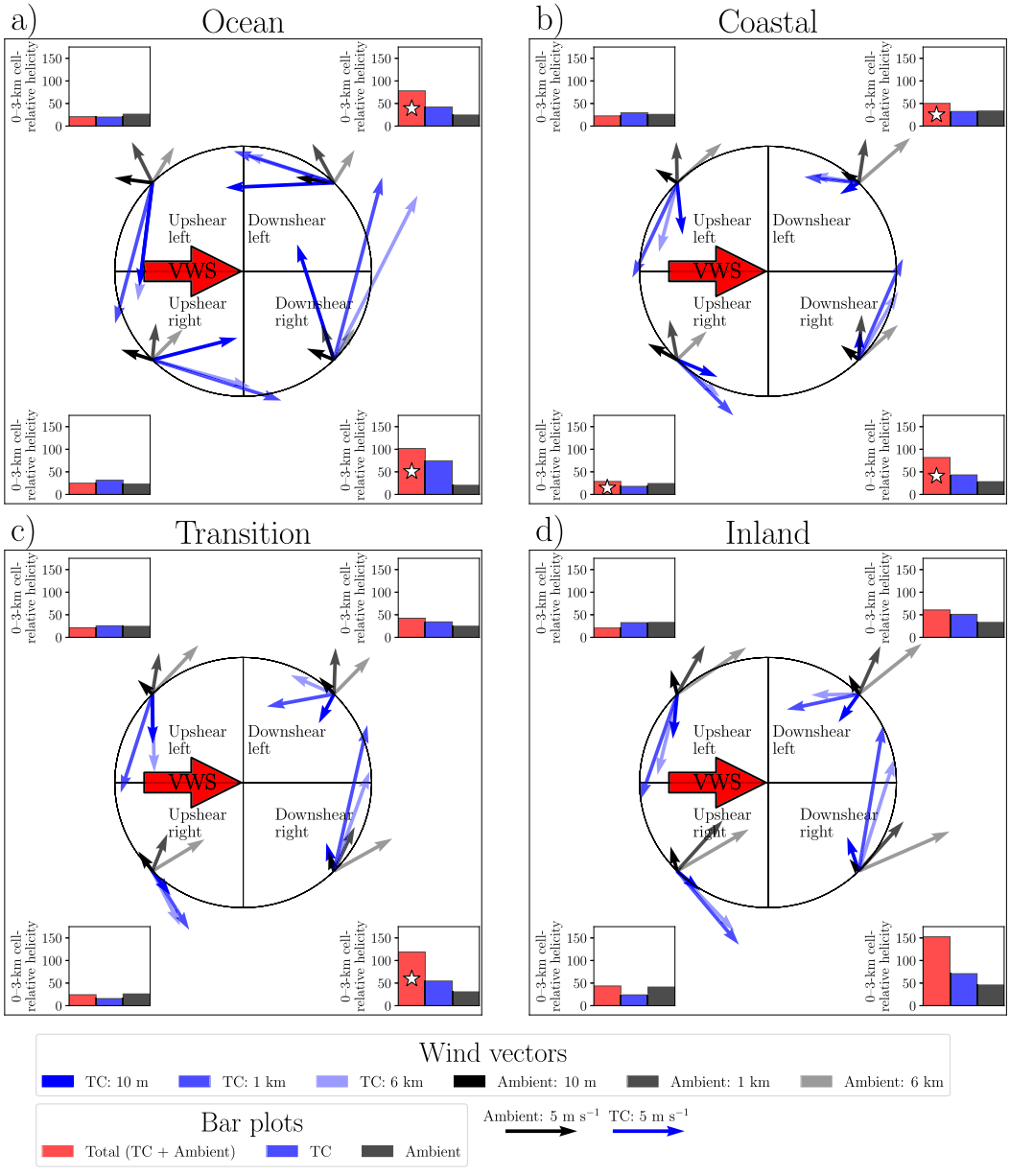

FIG. 17. Plan view plot of composite median 10-m, 1-km, and 6-km wind vectors ($m\,s^{-1}$) for the TC and ambient wind field, and bar plots of composite median 3-km convective cell-relative helicity ($m^2\,s^{-2}$) for the total (i.e., TC wind and ambient wind), TC, and ambient wind field in each VWS-relative quadrant of strongly sheared TCs in the (a) ocean, (b) coast, (c) transition, and (d) inland. The white stars denote quadrants in which the median helicity associated with the total wind field is statistically greater than that associated with the TC wind field at the 95% confidence interval. The radiosonde data are coarsened to the vertical grid spacing of the reanalysis data for these calculations.

of changes are statistically different at the 95% confidence interval.

The TC-relative asymmetries that develop in convective-scale thermodynamic environments with increasing distance from the coast may be due to the following:

- *Interaction between TC and baroclinic zone:* Inland convective-scale environments are associated with TCs that may more strongly interact with continental baroclinic zones. This baroclinic zone interaction yields the cyclonic advection and lateral entrainment of cool, dry air into the upshear quadrants, and warm, moist air into the downshear quadrants (Zawislak et al. 2016; Nguyen et al. 2017).
- *Greater distance from ocean:* The downshear-right quadrant typically partially overlaps with the southeast quadrant, which has

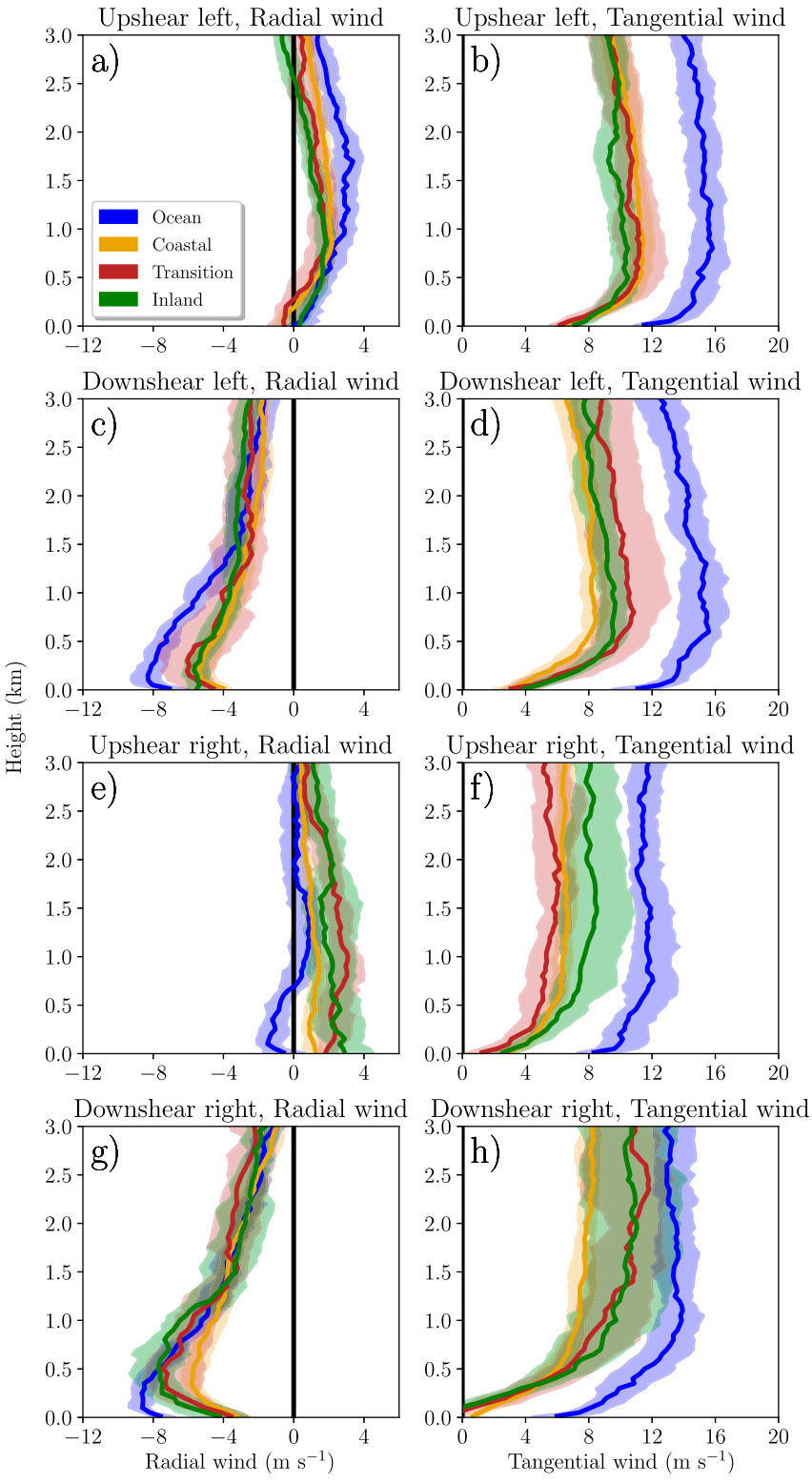

FIG. 18. Composite median (solid line) and its 95% confidence interval (shading) of vertical profiles of TC motion-relative (left) radial wind (m s^{-1}) and (right) tangential wind (m s^{-1}) computed from the dropsonde and radiosonde winds for strongly sheared TCs stratified by sondes in ocean, coastal, transition, and inland environments within the (a),(b) upshear-left; (c),(d) downshear-left; (e),(f) upshear-right; and (g),(h) downshear-right quadrants.

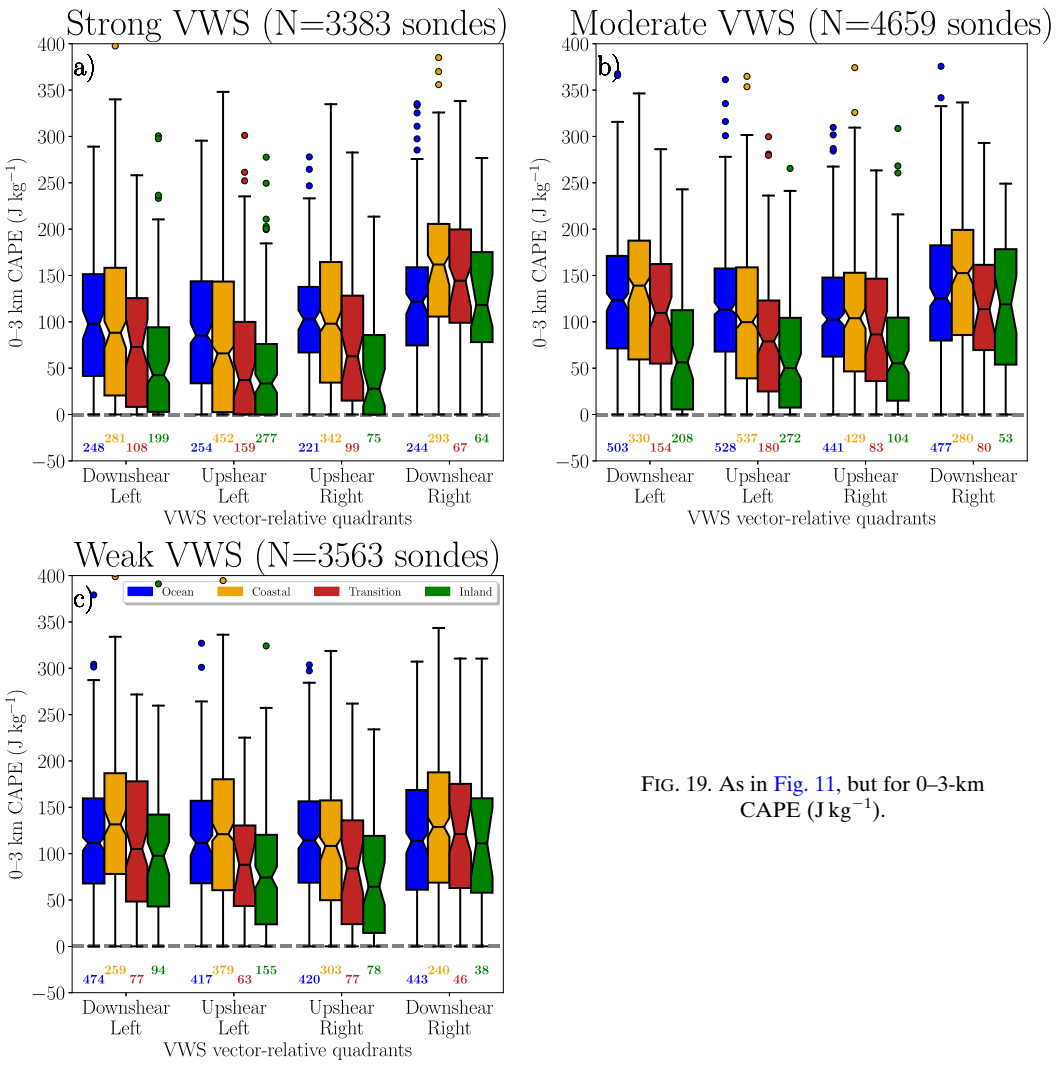

FIG. 19. As in Fig. 11, but for 0–3-km CAPE (J kg^{-1}).

the most direct access to warm, moist onshore flow. In contrast, the remaining quadrants typically have cooler, drier continental air sources (Corbosiero and Molinari 2003; Schenkel et al. 2020).

- *Cyclonic advection of convective downdrafts:* Convection strengthens in the downshear-right quadrant with increasing VWS, which produces stronger downdrafts that are cyclonically advected into the remaining three quadrants resulting in enhanced near-surface cooling and drying in the TC outer region (J. A. Zhang et al. 2013; DeHart et al. 2014). Without being offset by ocean surface fluxes, this cooling and drying are larger with increasing distance from the coast.

Each of these factors is plausible, but their importance is challenging to quantify using the observations studied here, necessitating a future modeling assessment.

Together, this study suggests a more nuanced response of convective-scale environments with increasing distance from the coast than suggested in prior work (McCaul 1991; Baker et al. 2009)—namely a strong dependence on VWS magnitude. In particular, the downshear-right quadrant of strongly sheared TCs is most kinematically and thermodynamically favorable for tornadoes and becomes even more kinematically supportive in inland environments despite TC intensity being weaker. In contrast, the remaining three quadrants in strongly sheared TCs, and all four quadrants, in both weakly and moderately sheared TCs, typically are less supportive of tornadoes. More generally, these results are consistent with the preference for tornadoes to transition from occurring in both downshear quadrants within all VWS regimes at the coast to within the downshear-right quadrant of strongly sheared TCs in inland environments. However, additional work is necessary to examine the environments associated with inner-core tornadoes occurring primarily in the downshear half of the TC, since the strong rotational inner-core winds preclude the analysis of dropsondes and radiosondes.

4. Summary and discussion

The present study analyzes how the response of TC tornado frequency and location, and convective-scale environments in coastal versus inland environments changes in response to

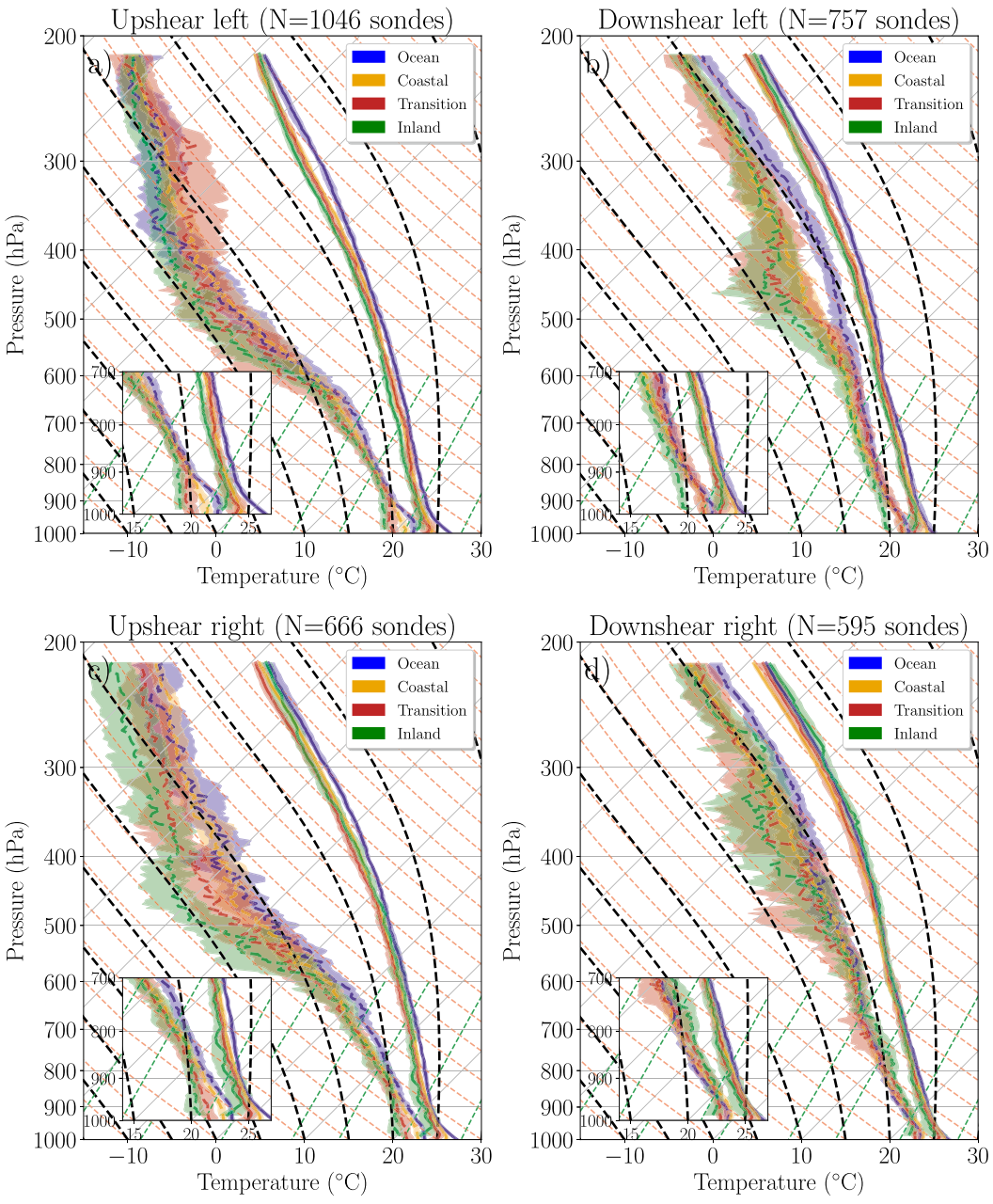

FIG. 20. Composite median skew T–log$p$ thermodynamic diagrams showing temperature (solid line), dewpoint (dashed line), and their 95% confidence interval (shading) computed from dropsondes and radiosondes in strongly sheared TCs stratified by sondes over the ocean, coastal, transition, and inland environments in the (a) upshear-left, (b) downshear-left, (c) upshear-right, and (d) downshear-right quadrants. The inset shows a magnified view of the 1000–700-hPa composite median temperature and dewpoint.

ambient deep-tropospheric (i.e., 850–200-hPa) vertical wind shear (VWS). To accomplish this, we first stratified multi-decadal tornado, dropsonde, and radiosonde data according to their distance from the coast. We further separated these data by reanalysis-derived VWS magnitude used to define weakly, moderately, and strongly sheared environments. We then analyzed how the frequency and location of TC tornadoes varied among these nine combinations of coastal and VWS regimes. To provide greater physical insight into these results, dropsondes and radiosondes were then used to diagnose the associated changes in convective-scale kinematic and thermodynamic environments.

This study shows that coastal tornadoes occur regardless of the VWS regime, with strongly sheared TCs most frequently producing tornadoes—including the most damaging ones. Moreover, the majority of inland tornadoes, especially more

damaging tornadoes, are produced by strongly sheared TCs. These inland tornadoes typically occur further poleward in association with strongly sheared TCs. With regards to their cyclone-relative location, coastal tornadoes primarily occur in the downshear sector most often with strongly sheared TCs. As the distance from the coast increases, tornadoes primarily occur in the outer region of the downshear-right quadrant in strongly sheared TCs.

Analysis of the convective-scale kinematic environments from radiosonde and dropsondes show that tornadic supercells are most strongly favored in the downshear-right quadrant of strongly sheared TCs—regardless of distance from the coast. Further analysis also suggests that coastal tornadoes are most strongly favored in the downshear-right quadrant of intense and/or large TCs in strong VWS. Moreover, as the distance from the coast increases, the downshear-right quadrant in strongly sheared TCs more distinctly favors tornadoes due to the stronger veering of the ambient winds and unexpectedly small changes in the TC outer winds, which constructively superimpose with one another. This former factor may favor tornadoes within a broader range of TC intensities and outer sizes. In contrast, both the remaining VWS-relative quadrants in strongly sheared TCs and all quadrants in weakly and moderately sheared TCs typically support tornadoes less.

Examination of convective-scale thermodynamic environments suggests that the downshear-right quadrant is consistently most favorable for tornadic supercells without consideration for the VWS regime or coastal location. While the remaining three VWS-relative quadrants in strongly sheared TCs thermodynamically support tornadoes at the coast, these quadrants become less favorable inland. Moderately sheared TCs show similar relationships, although the decreases in CAPE with increasing inland distance are more muted. In contrast, weakly sheared TCs are characterized by favorable tornadic supercell environments in each VWS-relative quadrant within all combinations of coastal and VWS regimes.

Together, these results suggest that the downshear-right quadrant of strongly sheared TCs is most favorable for tornadoes at the coast, and becomes increasingly favorable with greater distance inland. These favorable convective-scale environments may be due to a combination of vector superposition between the ambient and TC winds, and slow weakening of the TC outer winds after landfall. Building upon Schenkel et al. (2020), these results can be leveraged by forecasters to better identify:

- which TCs will potentially produce large numbers of tornadoes both at the coast and in inland environments;
- how TC-relative tornado location will change as the TC moves inland; and
- changes in convective-scale environments and convection as TCs move into inland environments.

Such guidance is critical given the multihazard threats associated with landfalling TCs, and the lower skill of tornado watches and warnings at all lead times compared to Great Plains supercells (Edwards 2012; Martinaitis 2017). However, further work is necessary to investigate the inner-core environments in strongly sheared TCs, which is unable to be investigated by radiosondes and dropsondes due to their rapid cyclonic advection by the strong inner-core winds. Moreover, the small sample size of radiosondes, especially in inland environments, precluded examining the radial variation in convective-scale environments, which also merits further investigation. Finally, future work should focus on how variability in the lower-tropospheric structure of VWS may impact tornado frequency and location given its importance to TC tornado production (McCaul 1991; Baker et al. 2009).

Acknowledgments. This study is generously supported by the NSF AGS-2028151, the University of Oklahoma, and the Cooperative Institute for Mesoscale Meteorological Studies (CIMMS). The statements, findings, conclusions, and recommendations herein are those of the authors and do not necessarily reflect the views of the NSF, University of Oklahoma, and NOAA. The authors thank Chris Landsea (TAFB), Matthew Bunkers (NWS), and two anonymous reviewers for their constructive comments. The authors would also like to thank Chris Nowotarski (TAMU), Eugene McCaul Jr. (USRA), Nusrat Yussouf (NSSL/OU), Lou Wicker (NSSL), Morris Weisman (NCAR), George Bryan (NCAR), Stan Trier (NCAR), Kate Young (NCAR), and John Knaff (CIRA) for insightful discussions. This work would not have been possible without the availability of TCTOR data from NOAA SPC, the ERA5 reanalysis from the ECMWF and the NCAR Research and Data Archive (European Centre for Medium-Range Weather Forecasts 2019), IBTrACS data from NOAA/NCDC, IGRA radiosonde data from NOAA, and NOAA/NASA/NSF dropsonde data from the NCAR EOL. All figures were made using Matplotlib (Hunter 2007) and MetPy (May et al. 2020). All kinematic and thermodynamic parameters were computed using SHARPpy (Blumberg et al. 2017).

Data availability statement. Subsetted SPC TCTOR tornado data can be obtained from the lead author. ERA-5 reanalysis data are available through the NCAR RDA website (https://rda.ucar.edu/datasets/ds633.0/). IBTRaCS data are available through the NCDC website (https://www.ncei.noaa.gov/data/international-best-track-archive-for-climate-stewardship-ibtracs/v04r00/access/netcdf/). Dropsonde data are available through the NCAR EOL website (https://www.eol.ucar.edu/observing_facilities/avaps-dropsonde-system). Radiosonde data from the IGRA v2 are available from (https://www.ncdc.noaa.gov/data-access/weather-balloon/integrated-global-radiosonde-archive).

REFERENCES

Aiyyer, A. R., and C. Thorncroft, 2006: Climatology of vertical wind shear over the tropical Atlantic. *J. Climate*, **19**, 2969–2983, https://doi.org/10.1175/JCLI3685.1.

Baker, A. K., M. D. Parker, and M. D. Eastin, 2009: Environmental ingredients for supercells and tornadoes within Hurricane Ivan. *Wea. Forecasting*, **24**, 223–244, https://doi.org/10.1175/2008WAF2222146.1.

Bian, G.-F., G.-Z. Nie, and X. Qiu, 2021: How well is outer tropical cyclone size represented in the ERA5 reanalysis

dataset? *Atmos. Res.*, **249**, 105339, https://doi.org/10.1016/j.atmosres.2020.105339.

Bieli, M., S. J. Camargo, A. H. Sobel, J. L. Evans, and T. Hall, 2019: A global climatology of extratropical transition. Part I: Characteristics across basins. *J. Climate*, **32**, 3557–3582, https://doi.org/10.1175/JCLI-D-17-0518.1.

Blake, E., and D. Zelinsky, 2018: Tropical cyclone report: Hurricane Harvey (17 August–1 September 2017). NHC Tech. Rep. AL092017, 77 pp., https://www.nhc.noaa.gov/data/tcr/AL092017_Harvey.pdf.

Blumberg, W. G., K. T. Halbert, T. A. Supinie, P. T. Marsh, R. L. Thompson, and J. A. Hart, 2017: SHARPpy: An open-source sounding analysis toolkit for the atmospheric sciences. *Bull. Amer. Meteor. Soc.*, **98**, 1625–1636, https://doi.org/10.1175/BAMS-D-15-00309.1.

Bogner, P. B., G. M. Barnes, and J. L. Franklin, 2000: Conditional instability and shear for six hurricanes over the Atlantic Ocean. *Wea. Forecasting*, **15**, 192–207, https://doi.org/10.1175/1520-0434(2000)015<0192:CIASFS>2.0.CO;2.

Brammer, A., 2017: Tropical cyclone vortex tracker. Accessed 7 November 2016, https://doi.org/10.5281/zenodo.266194.

——, and C. D. Thorncroft, 2017: Spatial and temporal variability of the three-dimensional flow around African easterly waves. *Mon. Wea. Rev.*, **145**, 2879–2895, https://doi.org/10.1175/MWR-D-16-0454.1.

Braun, S. A., and Coauthors, 2013: NASA's Genesis and Rapid Intensification Processes (GRIP) field experiment. *Bull. Amer. Meteor. Soc.*, **94**, 345–363, https://doi.org/10.1175/BAMS-D-11-00232.1.

——, P. A. Newman, and G. M. Heymsfield, 2016: NASA's Hurricane and Severe Storm Sentinel (HS3) investigation. *Bull. Amer. Meteor. Soc.*, **97**, 2085–2102, https://doi.org/10.1175/BAMS-D-15-00186.1.

Bunkers, M. J., B. A. Klimowski, J. W. Zeitler, R. L. Thompson, and M. L. Weisman, 2000: Predicting supercell motion using a new hodograph technique. *Wea. Forecasting*, **15**, 61–79, https://doi.org/10.1175/1520-0434(2000)015<0061:PSMUAN>2.0.CO;2.

——, D. A. Barber, R. L. Thompson, R. Edwards, and J. Garner, 2014: Choosing a universal mean wind for supercell motion prediction. *J. Oper. Meteor.*, **2**, 115–129, https://doi.org/10.15191/nwajom.2014.0211.

Cangialosi, J., A. Latto, and R. Berg, 2018: Tropical cyclone report: Hurricane Irma (30 August–12 September 2017). NHC Tech. Rep. AL112017, 111 pp., https://www.nhc.noaa.gov/data/tcr/AL112017_Irma.pdf.

Chavas, D. R., and K. Emanuel, 2010: A QuikSCAT climatology of tropical cyclone size. *Geophys. Res. Lett.*, **37**, L18816, https://doi.org/10.1029/2010GL044558.

——, and J. Vigh, 2014: QSCAT-R: The QuikSCAT tropical cyclone radial structure dataset. NCAR Tech. Note NCAR/TN-513+STR, 25 pp., https://doi.org/10.5065/D6J67DZ4.

Chen, J., and D. R. Chavas, 2020: The transient responses of an axisymmetric tropical cyclone to instantaneous surface roughening and drying. *J. Atmos. Sci.*, **77**, 2807–2834, https://doi.org/10.1175/JAS-D-19-0320.1.

Chen, S. S., J. A. Knaff, and F. D. Marks, 2006: Effects of vertical wind shear and storm motion on tropical cyclone rainfall asymmetries deduced from TRMM. *Mon. Wea. Rev.*, **134**, 3190–3208, https://doi.org/10.1175/MWR3245.1.

Corbosiero, K., and J. Molinari, 2002: The effects of vertical wind shear on the distribution of convection in tropical cyclones. *Mon. Wea. Rev.*, **130**, 2110–2123, https://doi.org/10.1175/1520-0493(2002)130<2110:TEOVWS>2.0.CO;2.

——, and ——, 2003: The relationship between storm motion, vertical wind shear, and convective asymmetries in tropical cyclones. *J. Atmos. Sci.*, **60**, 366–376, https://doi.org/10.1175/1520-0469(2003)060<0366:TRBSMV>2.0.CO;2.

Curtis, L., 2004: Midlevel dry intrusions as a factor in tornado outbreaks associated with landfalling tropical cyclones from the Atlantic and Gulf of Mexico. *Wea. Forecasting*, **19**, 411–427, https://doi.org/10.1175/1520-0434(2004)019<0411:MDIAAF>2.0.CO;2.

Davis, C., C. Snyder, and A. C. Didlake, 2008: A vortex-based perspective of eastern Pacific tropical cyclone formation. *Mon. Wea. Rev.*, **136**, 2461–2477, https://doi.org/10.1175/2007MWR2317.1.

DeHart, J. C., R. A. Houze, and R. F. Rogers, 2014: Quadrant distribution of tropical cyclone inner-core kinematics in relation to environmental shear. *J. Atmos. Sci.*, **71**, 2713–2732, https://doi.org/10.1175/JAS-D-13-0298.1.

DeMaria, M., and J. Kaplan, 1994: A Statistical Hurricane Intensity Prediction Scheme (SHIPS) for the Atlantic basin. *Wea. Forecasting*, **9**, 209–220, https://doi.org/10.1175/1520-0434(1994)009<0209:ASHIPS>2.0.CO;2.

Didlake, A. C., and R. A. Houze, 2009: Convective-scale downdrafts in the principal rainband of Hurricane Katrina (2005). *Mon. Wea. Rev.*, **137**, 3269–3293, https://doi.org/10.1175/2009MWR2827.1.

Ditchek, S. D., J. Molinari, K. L. Corbosiero, and R. G. Fovell, 2019: An objective climatology of tropical cyclone diurnal pulses in the Atlantic basin. *Mon. Wea. Rev.*, **147**, 591–605, https://doi.org/10.1175/MWR-D-18-0368.1.

Dunion, J., G. Wick, P. Black, and J. Walker, 2018: Sensing hazards with operational unmanned technology: 2015–2016 campaign summary, final report. NOAA Tech. Memo. OAR UAS-001, 49 pp., https://uas.noaa.gov/Portals/5/Docs/NOAA-UAS-Tech-Memo-1-SHOUT-Field-Campaigns-Summary_25Apr2018.pdf.

Durre, I., R. S. Vose, and D. B. Wuertz, 2006: Overview of the integrated global radiosonde archive. *J. Climate*, **19**, 53–68, https://doi.org/10.1175/JCLI3594.1.

Eastin, M. D., and M. C. Link, 2009: Miniature supercells in an offshore outer rainband of Hurricane Ivan (2004). *Mon. Wea. Rev.*, **137**, 2081–2104, https://doi.org/10.1175/2009MWR2753.1.

Edwards, R., 2010: Tropical cyclone tornado records for the modernized National Weather Service era. *25th Conf. on Severe Local Storms*, Denver, CO, Amer. Meteor. Soc., P3.1, https://ams.confex.com/ams/25SLS/techprogram/paper_175269.htm.

——, 2012: Tropical cyclone tornadoes: A review of knowledge in research and prediction. *Electron. J. Severe Storms Meteor.*, **7** (6), http://www.ejssm.org/ojs/index.php/ejssm/article/view/97/84.

——, and R. Thompson, 2012: Reversible CAPE in tropical cyclone tornado regimes. *27th Conf. on Severe Local Storms*, Madison, WI, Amer. Meteor. Soc., 88, https://ams.confex.com/ams/27SLS/webprogram/Paper254328.html.

——, A. R. Dean, R. L. Thompson, and B. T. Smith, 2012: Convective modes for significant severe thunderstorms in the contiguous United States. Part III: Tropical cyclone tornadoes. *Wea. Forecasting*, **27**, 1507–1519, https://doi.org/10.1175/WAF-D-11-00117.1.

——, J. G. LaDue, J. T. Ferree, K. Scharfenberg, C. Maier, and W. L. Coulbourne, 2013: Tornado intensity estimation: Past,

present, and future. *Bull. Amer. Meteor. Soc.*, **94**, 641–653, https://doi.org/10.1175/BAMS-D-11-00006.1.

Emory, A. E., M. McLinden, M. Schreier, and G. A. Wick, 2015: An introduction to the NASA east Pacific origins and characteristics of hurricanes (EPOCH) field campaign. *Trop. Cyclone Res. Rev.*, **4**, 124–131, https://doi.org/10.6057/2015TCRRh3.03.

European Centre for Medium-Range Weather Forecasts, 2019: ERA-Interim Reanalysis (0.25 Degree Latitude-Longitude Grid). National Center for Atmospheric Research, Computational and Information Systems Laboratory, accessed 7 September 2019, https://doi.org/10.5065/BH6N-5N20.

Finocchio, P. M., and S. J. Majumdar, 2017: A statistical perspective on wind profiles and vertical wind shear in tropical cyclone environments of the Northern Hemisphere. *Mon. Wea. Rev.*, **145**, 361–378, https://doi.org/10.1175/MWR-D-16-0221.1.

Foerster, A. M., M. M. Bell, P. A. Harr, and S. C. Jones, 2014: Observations of the eyewall structure of Typhoon Sinlaku (2008) during the transformation stage of extratropical transition. *Mon. Wea. Rev.*, **142**, 3372–3392, https://doi.org/10.1175/MWR-D-13-00313.1.

Frank, W. M., and E. A. Ritchie, 1999: Effects of environmental flow upon tropical cyclone structure. *Mon. Wea. Rev.*, **127**, 2044–2061, https://doi.org/10.1175/1520-0493(1999)127<2044:EOEFUT>2.0.CO;2.

Galarneau, T. J., and C. A. Davis, 2013: Diagnosing forecast errors in tropical cyclone motion. *Mon. Wea. Rev.*, **141**, 405–430, https://doi.org/10.1175/MWR-D-12-00071.1.

Gal-Chen, T., and R. C. Somerville, 1975: On the use of a coordinate transformation for the solution of the Navier-Stokes equations. *J. Comput. Phys.*, **17**, 209–228, https://doi.org/10.1016/0021-9991(75)90037-6.

Gentry, R. C., 1983: Genesis of tornadoes associated with hurricanes. *Mon. Wea. Rev.*, **111**, 1793–1805, https://doi.org/10.1175/1520-0493(1983)111<1793:GOTAWH>2.0.CO;2.

Green, B. W., F. Zhang, and P. Markowski, 2011: Multiscale processes leading to supercells in the landfalling outer rainbands of Hurricane Katrina (2005). *Wea. Forecasting*, **26**, 828–847, https://doi.org/10.1175/WAF-D-10-05049.1.

Hart, R., and J. Evans, 2001: A climatology of the extratropical transition of Atlantic tropical cyclones. *J. Climate*, **14**, 546–564, https://doi.org/10.1175/1520-0442(2001)014<0546:ACOTET>2.0.CO;2.

Hence, D. A., and R. A. Houze, 2008: Kinematic structure of convective-scale elements in the rainbands of Hurricanes Katrina and Rita (2005). *J. Geophys. Res.*, **113**, D15108, https://doi.org/10.1029/2007JD009429.

Hersbach, H., and Coauthors, 2020: The ERA5 global reanalysis. *Quart. J. Roy. Meteor. Soc.*, **146**, 1999–2049, https://doi.org/10.1002/qj.3803.

Hill, E., W. Malkin, and W. Schulz, 1966: Tornadoes associated with cyclones of tropical origin—Practical features. *J. Appl. Meteor.*, **5**, 745–763, https://doi.org/10.1175/1520-0450(1966)005<0745:TAWCOT>2.0.CO;2.

Hodges, K., A. Cobb, and P. L. Vidale, 2017: How well are tropical cyclones represented in reanalysis datasets? *J. Climate*, **30**, 5243–5264, https://doi.org/10.1175/JCLI-D-16-0557.1.

Houze, R. A., and Coauthors, 2006: The hurricane rainband and intensity change experiment: Observations and modeling of Hurricanes Katrina, Ophelia, and Rita. *Bull. Amer. Meteor. Soc.*, **87**, 1503–1522, https://doi.org/10.1175/BAMS-87-11-1503.

Hunter, J. D., 2007: Matplotlib: A 2D graphics environment. *Comput. Sci. Eng.*, **9**, 90–95, https://doi.org/10.1109/MCSE.2007.55.

Jones, S., 1995: The evolution of vortices in vertical shear. Part I: Initially barotropic vortices. *Quart. J. Roy. Meteor. Soc.*, **121**, 821–851, https://doi.org/10.1002/qj.49712152406.

Kaplan, J., and M. DeMaria, 1995: A simple empirical model for predicting the decay of tropical cyclone winds after landfall. *J. Appl. Meteor.*, **34**, 2499–2512, https://doi.org/10.1175/1520-0450(1995)034<2499:ASEMFP>2.0.CO;2.

Klein, P., P. Harr, and R. Elsberry, 2000: Extratropical transition of western North Pacific tropical cyclones: An overview and conceptual model of the transformation stage. *Wea. Forecasting*, **15**, 373–395, https://doi.org/10.1175/1520-0434(2000)015<0373:ETOWNP>2.0.CO;2.

Knaff, J. A., S. P. Longmore, and D. A. Molenar, 2014: An objective satellite-based tropical cyclone size climatology. *J. Climate*, **27**, 455–476, https://doi.org/10.1175/JCLI-D-13-00096.1.

Knapp, K. R., M. C. Kruk, D. H. Levinson, H. J. Diamond, and C. J. Neumann, 2010: The International Best Track Archive for Climate Stewardship (IBTrACS) unifying tropical cyclone data. *Bull. Amer. Meteor. Soc.*, **91**, 363–376, https://doi.org/10.1175/2009BAMS2755.1.

Knupp, K. R., J. Walters, and M. Biggerstaff, 2006: Doppler profiler and radar observations of boundary layer variability during the landfall of Tropical Storm Gabrielle. *J. Atmos. Sci.*, **63**, 234–251, https://doi.org/10.1175/JAS3608.1.

Landsea, C. W., and J. L. Franklin, 2013: Atlantic hurricane database uncertainty and presentation of a new database format. *Mon. Wea. Rev.*, **141**, 3576–3592, https://doi.org/10.1175/MWR-D-12-00254.1.

Marchok, T. P., 2002: How the NCEP Tropical Cyclone Tracker Works. *25th Conf. on Hurricanes and Tropical Meteorology*, San Diego, CA, Amer. Meteor. Soc., P1.13, https://ams.confex.com/ams/25HURR/techprogram/paper_37628.htm.

Markowski, P., C. Hannon, J. Frame, E. Lancaster, A. Pietrycha, R. Edwards, and R. L. Thompson, 2003: Characteristics of vertical wind profiles near supercells obtained from the Rapid Update Cycle. *Wea. Forecasting*, **18**, 1262–1272, https://doi.org/10.1175/1520-0434(2003)018<1262:COVWPN>2.0.CO;2.

Marks, F. D., R. A. Houze, and J. F. Gamache, 1992: Dual-aircraft investigation of the inner core of Hurricane Norbert. Part I: Kinematic structure. *J. Atmos. Sci.*, **49**, 919–942, https://doi.org/10.1175/1520-0469(1992)049<0919:DAIOTI>2.0.CO;2.

Martinaitis, S. M., 2017: Radar observations of tornado-warned convection associated with tropical cyclones over Florida. *Wea. Forecasting*, **32**, 165–186, https://doi.org/10.1175/WAF-D-16-0105.1.

May, R. M., S. C. Arms, P. Marsh, E. Bruning, J. R. Leeman, K. Goebbert, J. E. Thielen, and Z. S. Bruick, 2020: MetPy: A Python Package for Meteorological Data. Accessed 1 July 2018, https://doi.org/10.5065/D6WW7G29.

McCaul, E. W., 1991: Buoyancy and shear characteristics of hurricane-tornado environments. *Mon. Wea. Rev.*, **119**, 1954–1978, https://doi.org/10.1175/1520-0493(1991)119<1954:BASCOH>2.0.CO;2.

——, and M. L. Weisman, 1996: Simulations of shallow supercell storms in landfalling hurricane environments. *Mon. Wea. Rev.*, **124**, 408–429, https://doi.org/10.1175/1520-0493(1996)124<0408:SOSSSI>2.0.CO;2.

——, and ——, 2001: The sensitivity of simulated supercell structure and intensity to variations in the shapes of environmental

buoyancy and shear profiles. *Mon. Wea. Rev.*, **129**, 664–687, https://doi.org/10.1175/1520-0493(2001)129<0664:TSOSSS>2.0.CO;2.

——, D. E. Buechler, S. J. Goodman, and M. Cammarata, 2004: Doppler radar and lightning network observations of a severe outbreak of tropical cyclone tornadoes. *Mon. Wea. Rev.*, **132**, 1747–1763, https://doi.org/10.1175/1520-0493(2004)132<1747:DRALNO>2.0.CO;2.

Merrill, R., 1984: A comparison of large and small tropical cyclones. *Mon. Wea. Rev.*, **112**, 1408–1418, https://doi.org/10.1175/1520-0493(1984)112<1408:ACOLAS>2.0.CO;2.

Molinari, J., and D. Vollaro, 2008: Extreme helicity and intense convective towers in Hurricane Bonnie. *Mon. Wea. Rev.*, **136**, 4355–4372, https://doi.org/10.1175/2008MWR2423.1.

——, and ——, 2010: Distribution of helicity, CAPE, and shear in tropical cyclones. *J. Atmos. Sci.*, **67**, 274–284, https://doi.org/10.1175/2009JAS3090.1.

——, D. M. Romps, D. Vollaro, and L. Nguyen, 2012: CAPE in tropical cyclones. *J. Atmos. Sci.*, **69**, 2452–2463, https://doi.org/10.1175/JAS-D-11-0254.1.

Montgomery, M. T., and Coauthors, 2012: The Pre-Depression Investigation of Cloud-Systems in the Tropics (PREDICT) experiment: Scientific basis, new analysis tools, and some first results. *Bull. Amer. Meteor. Soc.*, **93**, 153–172, https://doi.org/10.1175/BAMS-D-11-00046.1.

Nguyen, L. T., R. F. Rogers, and P. D. Reasor, 2017: Thermodynamic and kinematic influences on precipitation symmetry in sheared tropical cyclones: Bertha and Cristobal (2014). *Mon. Wea. Rev.*, **145**, 4423–4446, https://doi.org/10.1175/MWR-D-17-0073.1.

Novlan, D. J., and W. M. Gray, 1974: Hurricane-spawned tornadoes. *Mon. Wea. Rev.*, **102**, 476–488, https://doi.org/10.1175/1520-0493(1974)102<0476:HST>2.0.CO;2.

Onderlinde, M. J., and D. S. Nolan, 2016: Tropical cyclone–relative environmental helicity and the pathways to intensification in shear. *J. Atmos. Sci.*, **73**, 869–890, https://doi.org/10.1175/JAS-D-15-0261.1.

Parker, M. D., 2014: Composite VORTEX2 supercell environments from near-storm soundings. *Mon. Wea. Rev.*, **142**, 508–529, https://doi.org/10.1175/MWR-D-13-00167.1.

Paterson, L. A., B. N. Hanstrum, N. E. Davidson, and H. C. Weber, 2005: Influence of environmental vertical wind shear on the intensity of hurricane-strength tropical cyclones in the Australian region. *Mon. Wea. Rev.*, **133**, 3644–3660, https://doi.org/10.1175/MWR3041.1.

Quinting, J. F., M. M. Bell, P. A. Harr, and S. C. Jones, 2014: Structural characteristics of T-PARC Typhoon Sinlaku during its extratropical transition. *Mon. Wea. Rev.*, **142**, 1945–1961, https://doi.org/10.1175/MWR-D-13-00306.1.

Ramsay, H. A., and C. A. Doswell III, 2005: A sensitivity study of hodograph-based methods for estimating supercell motion. *Wea. Forecasting*, **20**, 954–970, https://doi.org/10.1175/WAF889.1.

Rasmussen, E. N., 2003: Refined supercell and tornado forecast parameters. *Wea. Forecasting*, **18**, 530–535, https://doi.org/10.1175/1520-0434(2003)18<530:RSATFP>2.0.CO;2.

Reasor, P., M. Montgomery, and L. Grasso, 2004: A new look at the problem of tropical cyclones in vertical shear flow: Vortex resiliency. *J. Atmos. Sci.*, **61**, 3–22, https://doi.org/10.1175/1520-0469(2004)061<0003:ANLATP>2.0.CO;2.

Rios-Berrios, R., and R. D. Torn, 2017: Climatological analysis of tropical cyclone intensity changes under moderate vertical wind shear. *Mon. Wea. Rev.*, **145**, 1717–1738, https://doi.org/10.1175/MWR-D-16-0350.1.

Ritchie, E. A., and R. L. Elsberry, 2001: Simulations of the transformation stage of the extratropical transition of tropical cyclones. *Mon. Wea. Rev.*, **129**, 1462–1480, https://doi.org/10.1175/1520-0493(2001)129<1462:SOTTSO>2.0.CO;2.

Rogers, R., and Coauthors, 2006: The intensity forecasting experiment: A NOAA multiyear field program for improving tropical cyclone intensity forecasts. *Bull. Amer. Meteor. Soc.*, **87**, 1523–1538, https://doi.org/10.1175/BAMS-87-11-1523.

——, and Coauthors, 2013: NOAA'S hurricane intensity forecasting experiment: A progress report. *Bull. Amer. Meteor. Soc.*, **94**, 859–882, https://doi.org/10.1175/BAMS-D-12-00089.1.

Romps, D. M., and Z. Kuang, 2011: A transilient matrix for moist convection. *J. Atmos. Sci.*, **68**, 2009–2025, https://doi.org/10.1175/2011JAS3712.1.

Schenkel, B. A., and R. Hart, 2012: An examination of tropical cyclone position, intensity, and intensity life cycle within atmospheric reanalysis datasets. *J. Climate*, **25**, 3453–3475, https://doi.org/10.1175/2011JCLI4208.1.

——, N. Lin, D. Chavas, G. Vecchi, M. Oppenheimer, and A. Brammer, 2018: The lifetime evolution of outer tropical cyclone size. *J. Climate*, **31**, 7985–8004, https://doi.org/10.1175/JCLI-D-17-0630.1.

——, ——, ——, M. Oppenheimer, and A. Brammer, 2017: Evaluating outer tropical cyclone size in reanalysis datasets using QuikSCAT data. *J. Climate*, **30**, 8745–8762, https://doi.org/10.1175/JCLI-D-17-0122.1.

——, R. Edwards, and M. Coniglio, 2020: A climatological analysis of ambient deep-tropospheric vertical wind shear impacts upon tornadic supercells in tropical cyclones. *Wea. Forecasting*, **35**, 2033–2059, https://doi.org/10.1175/WAF-D-19-0220.1.

Schultz, L. A., and D. J. Cecil, 2009: Tropical cyclone tornadoes, 1950–2007. *Mon. Wea. Rev.*, **137**, 3471–3484, https://doi.org/10.1175/2009MWR2896.1.

Simpson, R., and H. Riehl, 1958: Midtropospheric ventilation as a constraint on hurricane development and maintenance. *Tech. Conf. on Hurricanes*, Miami Beach, FL, Amer. Meteor. Soc., D4-1–D4-10.

Spratt, S. M., D. W. Sharp, P. Welsh, A. Sandrik, F. Alsheimer, and C. Paxton, 1997: A WSR-88D assessment of tropical cyclone outer rainband tornadoes. *Wea. Forecasting*, **12**, 479–501, https://doi.org/10.1175/1520-0434(1997)012<0479:AWAOTC>2.0.CO;2.

Tang, B., and K. Emanuel, 2010: Midlevel ventilation's constraint on tropical cyclone intensity. *J. Atmos. Sci.*, **67**, 1817–1830, https://doi.org/10.1175/2010JAS3318.1.

——, and ——, 2012: A ventilation index for tropical cyclones. *Bull. Amer. Meteor. Soc.*, **93**, 1901–1912, https://doi.org/10.1175/BAMS-D-11-00165.1.

Thompson, R. L., R. Edwards, J. A. Hart, K. L. Elmore, and P. Markowski, 2003: Close proximity soundings within supercell environments obtained from the Rapid Update Cycle. *Wea. Forecasting*, **18**, 1243–1261, https://doi.org/10.1175/1520-0434(2003)018<1243:CPSWSE>2.0.CO;2.

Torn, R. D., and C. Snyder, 2012: Uncertainty of tropical cyclone best-track information. *Wea. Forecasting*, **27**, 715–729, https://doi.org/10.1175/WAF-D-11-00085.1.

Verbout, S. M., D. M. Schultz, L. M. Leslie, H. E. Brooks, D. Karoly, and K. L. Elmore, 2007: Tornado outbreaks associated with landfalling hurricanes in the North Atlantic Basin:

1954–2004. *Meteor. Atmos. Phys.*, **97**, 255–271, https://doi.org/10.1007/s00703-006-0256-x.

Wang, J., and Coauthors, 2015: A long-term, high-quality, high-vertical-resolution GPS dropsonde dataset for hurricane and other studies. *Bull. Amer. Meteor. Soc.*, **96**, 961–973, https://doi.org/10.1175/BAMS-D-13-00203.1.

Wessel, P., and W. H. Smith, 1996: A global, self-consistent, hierarchical, high-resolution shoreline database. *J. Geophys. Res.*, **101**, 8741–8743, https://doi.org/10.1029/96JB00104.

Zawislak, J., H. Jiang, G. R. Alvey III, E. J. Zipser, R. F. Rogers, J. A. Zhang, and S. N. Stevenson, 2016: Observations of the structure and evolution of Hurricane Edouard (2014) during intensity change. Part I: Relationship between the thermodynamic structure and precipitation. *Mon. Wea. Rev.*, **144**, 3333–3354, https://doi.org/10.1175/MWR-D-16-0018.1.

Zhang, J., R. Lindsay, A. Schweiger, and M. Steele, 2013: The impact of an intense summer cyclone on 2012 Arctic sea ice retreat. *Geophys. Res. Lett.*, **40**, 720–726, https://doi.org/10.1002/grl.50190.

Zhang, J. A., R. F. Rogers, P. D. Reasor, E. W. Uhlhorn, and F. D. Marks, 2013: Asymmetric hurricane boundary layer structure from dropsonde composites in relation to the environmental vertical wind shear. *Mon. Wea. Rev.*, **141**, 3968–3984, https://doi.org/10.1175/MWR-D-12-00335.1.